EFFECT OF INTERNAL HYDROGEN ON THE TENSILE PROPERTIES OF DIFFERENT CrMo(V) STEEL GRADES: INFLUENCE OF VANADIUM ADDITION ON HYDROGEN TRAPPING AND DIFFUSION

L.B.Peral, A. Zafra, I. Fernández-Pariente, C.Rodríguez and J.Belzunce

Department of Materials Science and Metallurgical Engineering, University of Oviedo, Campus Universitario, East Building, 33203, Gijón, Spain

Corresponding author: luisborjapm@gmail.com (L.B.Peral)

Abstract: The influence of hydrogen on the mechanical behaviour of different quenched and tempered CrMo steels with or without vanadium were investigated by means of tensile tests. Smooth and circunferentially-notched round-bar specimens pre-charged with gaseous hydrogen in a high pressure hydrogen reactor were tested. The degradation of the tensile properties was correlated with the interaction between hydrogen atoms and microstructure, which was analyzed by means of thermal desorption analysis (TDA) and permeation tests. A LECO DH603 hydrogen analyser was used to study the activation energies of the different microstructural traps and also to study the hydrogen eggresion kinetics at room temperature. Moreover, electrochemical hydrogen permeation tests were also used to determine the apparent hydrogen diffusion coefficients and the density of traps present in the different steel grades.
Hydrogen embrittlement measured in notched specimens was much greater than that observed in the smooth samples, being this effect more notable in the steel grades with higher yield strengths, tempered at the lowest temperatures, where a change in the fracture micromechanism from ductile in the absence of hydrogen to intermediate and brittle in the presence of internal hydrogen was clearly observed, especially in tests performed at the lowest displacement rates. Results were discussed through FEM simulations of local stresses acting on the process zone. On the other hand, the V-added steel grades were less sensitive to hydrogen embrittlement due to the effect of the submicrometric VC precipitated during the tempering treatment, which might be considered non-diffusible hydrogen-trapping sites, in view of their strong hydrogen-trapping capability (35-41 kJ/mol). In these steels (V-added grades), diffusible hydrogen and hydrogen accumulation in the process zone decrease, improving hydrogen embrittlement resistance.

Keywords: hydrogen embrittlement, notch tensile tests, thermal desorption analysis, electrochemical hydrogen permeation tests, CrMo steels.

1 Introduction

A certain number of pressing technical problems must be solved for the development of infrastructures able to deal with the expected hydrogen society in the near future. In this context, it is important to understand the complex embrittlement phenomena due to the presence of hydrogen that may result in a significant degradation of the mechanical properties of metallic materials. Vessels and pipelines used to store and transport hydrogen must be able to provide a safe service during long periods of time in direct contact with gaseous hydrogen under high internal pressure, being then essential to ensure good resistance to hydrogen embrittlement (HE). Generally, quenched and tempered steels alloyed with chromium, chromium-molybdenum or chromium-molybdenum-vanadium are used in these industrial facilities [1]. In order to reduce the vessel wall thickness and hence the cost of the components, medium and high strength steels are preferred, although it is well known that these steels are more sensitive to hydrogen embrittlement than low strength ferritic steels, austenitic stainless steel or aluminium alloys [2-4]. This susceptibility increasing with the strength level of the steels [3-9]. The family of quenched and tempered chromium-molybdenum-vanadium steels may be tempered at relatively high temperature in order to reduce strength and hardness, so as to reduce hydrogen embrittlement problems. Moreover, the effect of ‘hydrogen

trapping' plays an important role in hydrogen embrittlement. Hydrogen atoms are known to be retained in quenched and tempered steels (tempered martensite microstructures) in microstructural traps, such as prior austenitic grain boundaries, martensitic lath and packet interfaces, dislocations, matrix-precipitated carbide interfaces (cementite in the case of the non-alloyed steels) and matrix-inclusion interfaces.

When a notched component is submitted to an external load for long periods of time in a hydrogen environment, hydrogen atoms diffuse along the steel microstructure and accumulate at the stress concentration region located in front of the notch (high triaxiality). Hydrogen concentration in the region located ahead of the notch in medium and high strength steels is dominated by the hydrostatic stress and can be estimated according to the Oriani theory by means of equation 1 [10].

$$C_{H\text{-notch}} = H_D \exp\left(\frac{\sigma_H \cdot V_H}{R \cdot T}\right) \quad (1)$$

Where $C_{H\text{-notch}}$ is the hydrogen concentration in the vicinity of the notch, H_D the diffusible hydrogen content (lattice and reversible hydrogen), σ_H is the hydrostatic stress developed in the notch region, V_H is the partial molar volume of hydrogen in BCC Fe (V_H=2.1·10^{-6} m^3/mol), R the gas constant and T is the testing temperature.

Due to the accumulation of hydrogen in this area, a critical hydrogen concentration can be reached, giving rise to embrittlement mechanisms responsible for a premature failure. In this way, the homogeneous distribution of strong traps in the microstructure of the steel might contribute to delay hydrogen diffusion, reducing hydrogen accumulation in the process zone improving the hydrogen embrittlement resistance. At this respect, the addition of vanadium to chromium-molybdenum steels to estimulate the precipitation of vanadium carbides during the tempering was demonstrated to be a good practice in order to fight against hydrogen embrittlement. Different authors have proved that vanadium carbides act as strong hydrogen traps [11-14]. This fact is illustrated in Figure 1 in a notched specimen submited to a tensile load in the presence of internal hydrogen

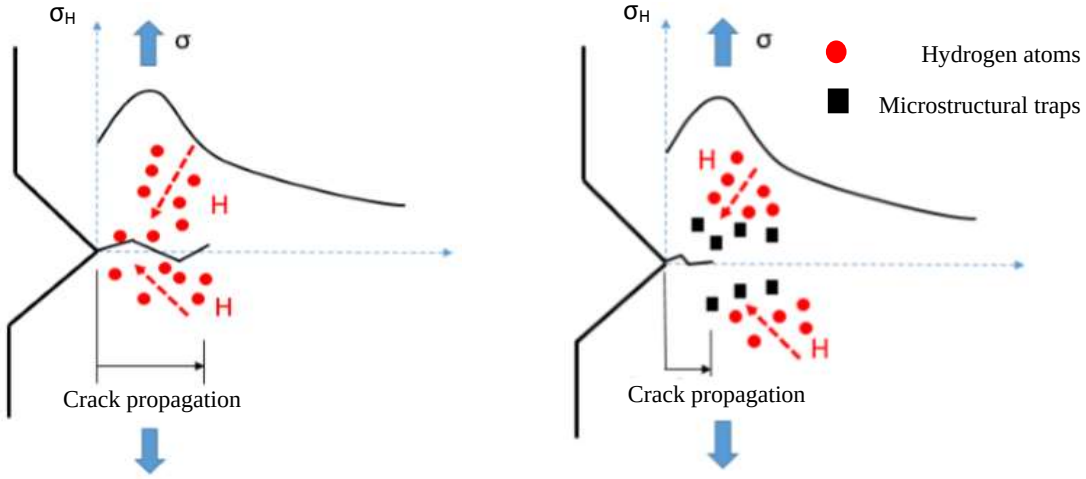

(a) *(b)*

Figure 1. Notched tensile specimen. Hydrogen diffusion towards the stress concentrator. (a) Without traps. (b) With traps

Consequently, different authors have studied the 'hydrogen trapping' effect in different steel microstructures and have determined the activation energies of the different traps present in quenched and tempered steels. Table 1 shows results extracted from the literature, with the corresponding references.

Dislocations (elastic field)	20-30[15], 23-27[16], 26[17], 24-27[18]
Dislocation cores	59[15], 60[16], 60-61[18], 59[19]
Prior austenitic grain boundaries	32[16], 18-20[17], 17-59[18], 26 [19], 18.3 [20]
α /Fe_3C interfaces	11-18[16], 18.3[19], 8.4-13.4[21]
α/MnS interfaces	72[15], 72.3[17]
Vanadium carbides	32.6 [11], 35.3 [11], 36[12], 27.4 [13]

Table 1. Activation energies (kJ/mol) of typical hydrogen traps present in steels

Then, although the embrittlement effects of hydrogen on chromium-molybdenum-vanadium steels and on other quenched and tempered steels have been studied for some time now, the operative hydrogen embrittlement mechanisms are still controversial. Moreover, in most studies, the hydrogen content in the steels have not been directly measured and the hydrogen effect on the mechanical properties measured by means of typical hydrogen embrittlement indexes have not been directly correlated to the interaction between hydrogen atoms and the steel microstructure using parameters as the trap energy, density of traps or apparent hydrogen diffusion coefficient. Moreover, it is nowadays known that mechanical loads, hydrogen uptake and trapping, hydrogen diffusion and microstructure are all involved on the embrittlement mechanisms. In this sense, many theories have been proposed to explain the mechanisms of hydrogen embrittlement on structural steels. Namely, the two most generally accepted ones are the Hydrogen-Enhanced-Decohesion (HEDE) [22-24] and the Hydrogen-Enhanced-Localized-Plasticity (HELP) [24-26]. The mechanisms of hydrogen induced failure in quenched and tempered steels usually starts with the stress activation of slip systems in individual grains at stress concentrators, being nowadays accepted that the enhancement of this dislocation activity is explained due to the HELP mechanism. As a result, the mobility of dislocations increases and plasticity localizes due to the presence of hydrogen [26-28]. Nucleation, growth and coalescence of microvoids is facilitated, resulting in a fracture surface characterized by the presence of large and shallow dimples. Under higher local loads or in the case of high strength steels, HEDE mechanism predominates. HEDE mechanism supposes that hydrogen atoms adsorbed or segregated at internal interfaces and grain boundaries weaken the interatomic bonds and cause decohesion under relatively low local loads [29], leading to brittle or quasi-brittle fractures, such as a cleavage or intergranular decohesion along prior austenitic grain boundaries or along interfaces between martesnsitic laths and packets, promoted by carbides precipitation and segregation of residual elements. Although it is argued that only diffusible hydrogen reduces the interface cohesion [30], the mechanical properties degradation due to hydrogen is also influenced by other variables such as the geometry and dimensions of the specimens or by testing parameters as, for example, the strain rate [3].

In this context, smooth and circumferentially-notched specimens of quenched and tempered 2.25Cr1Mo and 2.25Cr1MoV steels were thermally pre-charged with gaseous hydrogen in a high pressure hydrogen reactor and the tensile properties on smooth and notched samples were determined and compared under different applied displacement rates to analyse the influence of the strain rate and stress concentrators on hydrogen embrittlement. Gaseous hydrogen pre-charging at high temperature is a very effective method as, given the exponential vatiation of the diffusion coefficient and solubility with temperature, the kinetics of hydrogen entry into the steel is significantly accelerated and, after a few hours, a similar concentration of hydrogen to that obtained after years of service at room temperature can be reached. Other objectives of this work were to analyse the influence of the steel yield strength (produced modifying the tempering temperature) and the addition of vanadium (vanadium free and vanadium added steels) on the hydrogen embrittlement susceptibility of the steels. Moreover, thermal desorption analysis and electrochemical hydrogen permeation tests were used to analyse the interaction hydrogen/microstructure on the different heat treated steels in order to explain the effect of hydrogen on the mechanical properties of the different steel grades. In addition, FEM simulations of the notched tensile tests was carried out and a thorough fractographic analysis was performed to identify the operative failure micromechanisms.

2 Experimental procedure

2.1 Materials, heat treatments and specimens

Two different low-alloyed ferritic steels from the Cr-Mo family were selected in this study, with and without vanadium. The chemical composition of the steels, in weight %, is shown in Table 2.

Steel grade	C	Mn	Si	P	S	Cr	Mo	Ni	V
2.25Cr1Mo	0.143	0.563	0.157	0.005	0.0020	2.23	1.00	0.090	-
2.25Cr1MoV	0.150	0.520	0.086	0.006	0.0016	2.27	1.06	0.186	0.31

Table 2. Chemical composition of 2.25Cr1Mo and 2.25Cr1MoV steels (weight %)

2.25Cr1Mo and 2.25Cr1MoV steels were studied in the as-received (AR) condition (see Table 3). In addition, 2.25Cr1Mo steel was austenitized at 940ºC for 30 min, quenched in water and tempered at 600ºC for two hours. Regarding 2.25Cr1MoV, it was austenitized at 940ºC for 30 min, quenched in water and tempered at 650ºC for two hours. In this way, two different grades with the same chemical composition were obtained in each case. The sequence of heat treatments and the nomenclature of the obtained grades (based on the tempering temperature) are shown in Table 3.

	Specimen ID	Heat treatment sequences
V-free	2.25Cr1Mo_690	AR: 940ºC/3h+ water quenched + 690ºC/30h tempered
	2.25Cr1Mo_600	AR+940ºC/30min+water quenched+600ºC/2h tempered
V-added	2.25Cr1MoV_720	AR: 925ºC/90min+ water quenched + 720ºC/3h tempered
	2.25Cr1MoV_650	AR+940ºC/30min+water quenched +650ºC/2h tempered

Table 3. Applied heat treatments (on plates of 12 mm thickness)

Different specimens were machined to perform the different mechanical tests: small cylindrical samples (Figure 2c) were used to measure hydrogen content introduced into the different steel grades and to study the kinetics of hydrogen egression at room temperature (RT). The same geometry was employed to determine the activation energy of microstructural hydrogen traps. Electrochemical hydrogen permeation technique was applied onto small plates with 1 mm thickness (Figure 2d). Finally, smooth tensile specimens (Figure 2a) and notched tensile specimens with a sharp notch (Figure 2b) were also machined. In these cases, the tensile load was always applied perpendicular to the rolling direction (L) as can be seen in Figure 2.

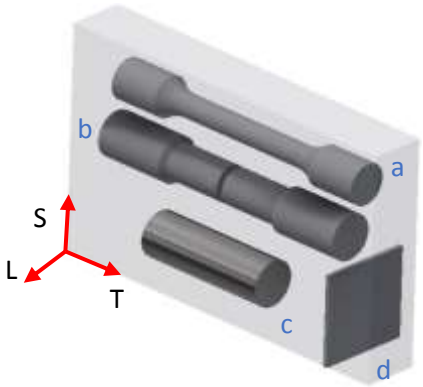

Figure 2. Test samples machined from the heat treated plates (12 mm thickness). L: rolling direction, T: transversal direction, S: thickness direction

2.2 Microstructure and hardness

The steel microstructures were observed in a scanning electron microscope (SEM JEOL-JSM5600) using an acceleration voltage of 20 kV. Previously, the samples were ground and finally polished with 1µm

diamond paste and etched with Nital-2%. The metallographic prepared samples were also employed to determine the dislocation density and residual stresses.

Brinell hardness (HB) was also determined using a Hoytom hardness tester using a load of 187.5 kg and a ball of 2.5 mm diameter, according to [31]. On each case, five measuremens were conducted and the average value was determined.

2.2.1 Dislocation density

The dislocation density in the 2.25Cr1Mo(V) steel grades after the different heat tratments was experimentally measured using the Williamson-Hall method [32], based on the full width half maximum (FWHM). These measurements were carried out by means of an X-ray Stresstech 3000-G3R diffactometer with K_α chromium radiation at 30 kV and 6.7 mA. The FWHM parameter was calculated in different 2Θ(°) positions corresponding to the following martensite/ferrite diffraction planes: $\{211\}_{2\Theta=156.4^\circ}$, $\{200\}_{2\Theta=106.1^\circ}$ and $\{110\}_{2\Theta=69^\circ}$. These data were analysed using the Williamson-Hall equation (equation 2):

$$FWHM_{corrected}\frac{\cos(\theta)}{\lambda} = \frac{0.9}{D} + 2\varepsilon\frac{\sin(\theta)}{\lambda} \quad (2)$$

Where Θ is the diffraction angle, λ the X-ray wave-length (λ = 0.2291 nm), D the average particle size and $FWHM_{corrected}$ the corrected full width half maximum. The dislocation density, ρ, was calculated using equation 3, where ε can be calculated from the slope of FWHM·cos(Θ)/λ versus sin(Θ)/λ plot, equation 2.

$$\rho = 14.4\left(\frac{\varepsilon}{b}\right)^2 \quad (3)$$

Where b is the Burgers vector (b=0.248 nm) [33].

The FWHM measurements obtained on the different peaks ($FWHM_{initial}$) were corrected taking into consideration the instrumental broadening ($FWHM_{instrumental}$). $FWHM_{instrumental}$ was measured in a specimen with a large grain size [34]. With this aim, a sample of 2.25Cr1MoV_720 steel grade was austenitized at 940°C for 30 minutes and then slowly cooled in the furnace (annealed sample). The corrected FWHM ($FWHM_{corrected}$) was then determined by means of equation 4.

$$FWHM^2_{corrected} = FWHM^2_{initial} - FWHM^2_{instrumental} \quad (4)$$

2.2.2 Residual stresses

Residual stresses were measured using the aforementioned Stresstech 3000-G3R X-ray diffractometer. The Kα chromium wavelength was employed onto the {211} ferrite/martensite planes under a 2Θ angle of 156.4º. The residual stress was determined using the $\sin^2\psi$ technique by means of equation 5 [35].

$$\sigma_\phi = \left(\frac{E}{1+\nu}\right)_{(hkl)}\left(\frac{1}{d_{\phi 0}}\right)\left(\frac{\partial d_{\phi\psi}}{\partial \sin^2\psi}\right) \quad (5)$$

Where, E and v are the elastic modulus and Poisson coefficient of the steel along the crystallographic direction of measurement, d is the interplanar distance of the selected diffraction plane (hkl), ψ the tilt angle and ϕ the angle in the sample plane. Values of E=211000 MPa and v=0.3 were used. The detection of the diffraction peak was carried out at nine positions of the tilt angle, between -45 and +45º, using an exposure time of 40 seconds in each position. The working parameters used for the measurement of residual stresses are shown in Table 4.

Measurement mode	Modified χ	Filter of the K_α radiation	Vanadium
Maximum voltage (V)	30	Maximum intensity (mA)	6.7
Exposure time (s)	50	Ø colimator (mm)	1
Tilt ψ (º)	9 points between -45°/+45°	Goniometric rotation (measurement direction) φ (º)	0
Noise reduction	Parabolic	Peak adjustment	Pseudo-Voigt

Table 4. Working parameters used for residual stress measurements

2.3 Fracture surface observations

The fracture surfaces of the tested specimens were also carefully examined using the already mentioned Scanning Electron Microscope under different magnifications.

2.4 Hydrogen pre-charging

All the specimens were pre-charged with gaseous hydrogen in a high-pressure reactor with a diameter of 73 mm and total length of 180 mm, manufactured in accordance with the ASTM G146 standard [36]. In order to make sure that the specimens were saturated with hydrogen, the following conditions were applied: 21 hours at 450ºC under a pressure of 19.5 MPa of pure hydrogen. After the maintenance time, a cooling phase of 1 hour, until a temperature of 85ºC (keeping the hydrogen pressure at 19.5 MPa to minimize hydrogen departure) was always used. Afterwards, the hydrogen pre-charged specimens were removed from the reactor and rapidly immersed in liquid nitrogen (-196ºC), where they were kept until the moment of testing, in order to limit hydrogen losses.

2.5 Hydrogen content and hydrogen desorption curves measurements

Being one of the aims of the study to correlate the loss of mechanical properties with the amount of hydrogen present in the different steel grades, the hydrogen egression kinetics at room temperature was determined. With this purpose, cylindrical pins with a diameter of 10 mm and a length of 30 mm were used (≈ 20g), see Figure 2c.

The hydrogen content of the samples was measured in a LECO DH603 analyzer, which is able to measure hydrogen concentrations between 0.1 and 2500 ppm. The measuring principle of the equipment is based on the difference of thermal conductivity between a reference gas flow of pure nitrogen and a secondary flow carrying nitrogen and the hydrogen extracted from the specimen. This conductivity difference is measured by means of a Wheatstone bridge and converted into an electrical signal that is interpreted by the equipment software, which finally gives the sample hydrogen concentration in 'ppm'.

The procedure to obtain the desorption curves was the following: all the cylindrical hydrogen pre-charged pins were removed from the liquid nitrogen at the same time, and exposed in air at room temperature. Then, the hydrogen concentration of the samples was measured at different time intervals. Before starting the measure, each sample was cleaned in an ultrasonic bath with acetone for 5 minutes, and then carefully dried using cold air. The analysis to determine hydrogen concentration consists on keeping the sample at 1100ºC during approximately 400 seconds in the aforementioned LECO DH603 analyzer.

2.6 Determination the activation energy of hydrogen traps

To determine the hydrogen trapping characteristics in the different steel grades, hydrogen measurements were performed in the hydrogen LECO DH603 analyzer under different heating rates (3600, 2400, 1800, 1200, 800 and 400ºC/h) for determining the activation energy of hydrogen traps present in the microstructure of the steels. Assuming that the escape of hydrogen from a trap site is a thermally activated process, the hydrogen evolution rate from trapping sites can be written according to the following expression (Equation 6).

$$\frac{dX_H}{dt} = A \cdot (1\text{-}X_H) \cdot \exp(-E_a/RT) \qquad (6)$$

Where X_H is the fraction of hydrogen evolved from a trapping site characterized by an activation energy E_a, being A a constant.

Hence, when a hydrogen-charged specimen is heated at a uniform rate, $\phi_i \cdot (dT/dt)$, a hydrogen peak, related to the trap activation energy, is detected at a certain temperature, T_{p_i}. Using the model developed by Lee and Lee [17], the trap activation energy, E_a, can be calculated from the slope of a $\ln(\phi_i/T_{p_i}^2)$ versus $1/T_{p_i}$ plot, Equation 7. A linear regression is then defined measuring the change in the peak temperature with the applied heating rate.

$$\frac{d\left[Ln\left(\frac{\phi i}{T_{p_i}^2}\right)\right]}{d\left(\frac{1}{T_{p_i}}\right)} = -\frac{E_a}{R} \qquad (7)$$

2.7 Electrochemical hydrogen permeation tests

Hydrogen absorption, permeation and diffusion was analysed using the electrochemical double cell, which was first proposed by Devanathan and Stachurski [37]. Hydrogen atoms are generated on the charging cell (the entry side of the steel membrane) and the diffusing hydrogen atoms are oxidized on the anodic cell (exit side). Accordingly, an anodic current density (J) was continuosly recorded using an Ivium PocketSTAT potenciostat. On the entry side, hydrogen was generated under a current density of 1 mA/cm^2 (in galvanostatic conditions) using a 2 mol/l H_2SO_4 + 0.25 g/l of As_2O_3 solution (pH=1). This small current density is enough to ensure that hydrogen available in the solution, H^+, is reduced and partially adsorbed in the steel surface, allowing hydrogen diffusion along the thickness of the steel membrane, and its arrival to the exit side can be registered as an anodic current evolution. A circular area of approximately 1 cm^2 was exposed to the solution and the electrochemical tests were conducted at room temperature (~20°C).

The anodic cell (the hydrogen exit side) contained 0.1 mol/l NaOH solution (pH=12) and was potentiostatically polarized at a constant potential of 50 mV versus a silver/silver-chloride (Ag/Ag-Cl) reference electrode (Ref). The steel samples were electrolytically coated with palladium on the anodic side prior to the test to facilitate hydrogen oxidation. Figure 3 displays the schematic Devanathan-Stachurski double cell empoyed in this study.

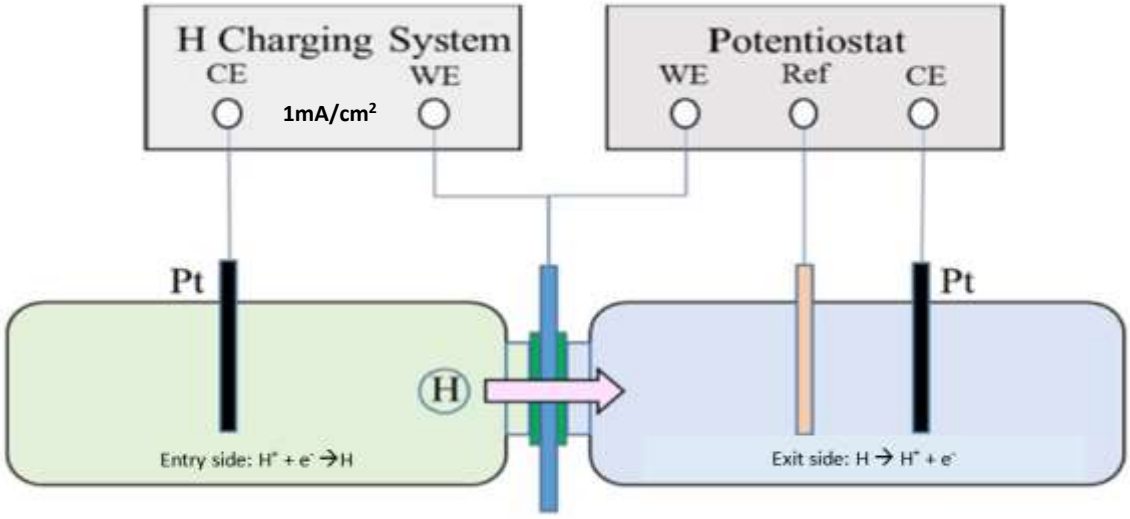

Figure 3. Devanathan-Stachurski double cell. CE: counter electrode (Pt), WE: working electrode (steel sample) and Ref: reference electrode (Ag/Ag-Cl)

The apparent diffusion coefficient was calculated using the 'time lag' method derived from Fick´s second law [38] by means of equation 8.

$$D_{app} = \frac{L^2}{6 \cdot t_L} \qquad (8)$$

Where L is the thickness of the sample and t_L is the time lag or time to attain J=0.63J_{max}, being J the current density and J_{max} the current density corresponding to the steady state.

The hydrogen concentration of the subsurface at the entry or cathodic side, C_{app}, can be estimated by equation 9 [38, 39], where M_H is the molar mass of hydrogen (1g/mol), F the Faraday constant (96485 C/mol) and ρ_{Fe} the density of iron ($7.87 \cdot 10^6$ g/m^3).

$$C_{app} = \frac{J_{max} \cdot M_H \cdot L}{D_{app} \cdot F \cdot \rho_{Fe}} \quad (9)$$

Equation 10 is the result of a mathematical model [39] that can be used to determine the average density of hydrogen traps (N_T) present in the steel microstructure, only needing the results obtained in the permeation test. N_A is the Avogadro´s constant ($6.022 \cdot 10^{23}$ mol^{-1}).

$$N_T = \frac{C_{app}}{3} \cdot \left(\frac{D_{Lattice}}{D_{app}} - 1\right) \cdot N_A \quad (10)$$

To estimate the lattice diffusion coefficient ($D_{Lattice}$) in the different steel grades, a decay transient was applied once the steady state hydrogen flux was achieved (switching-off of the cathodic current). According to Zakroczymski [40] and Frappart [41], in the initial part of the decay curve ($1 \geq i/i_\infty \geq 0.9$), desorption of diffusible hydrogen prevails and this part of the cuve is well described by the theoretical Fick´s law, equation 11, allowing us to estimate the hydrogen lattice diffusion, $D_{Lattice}$.

$$\frac{i}{i_\infty} = 1 - \frac{2}{\sqrt{\pi \cdot \tau}} \sum_{n=0}^{\infty} exp\left(-\frac{(2n+1)^2}{4\tau}\right) \quad (11)$$

Where: $\tau = \frac{D_{Lattice} \cdot t}{L^2}$

2.8 Tensile tests

Tensile tests on smooth and circumferentially-notched round-bar specimens, whose dimensions and geometries are shown in Figure 4, were performed on an Instron 5582 tensile testing machine. All uncharged tests were performed at 0.4 mm/min, but different displacement rates (from 0.4 to 0.0004 mm/min) were applied in the case of the pre-charged specimens in order to study the influence of this important parameter in hydrogen embrittlement. The stress concentration factor of the notched tensile specimen, with a notch root radius of 0.15 mm and a cross-section radius of 5 mm, was calculated by means of FEM analysis. A stress concentration factor around K_t=4.25 was obtained. This value is in agreement with those calculated by other authors using similar specimen geometries [3].

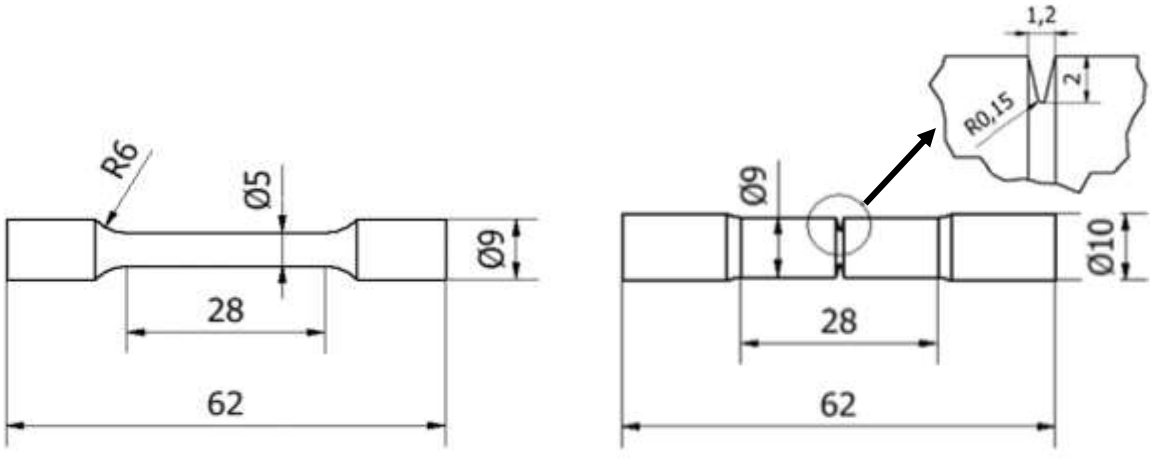

(a) (b)

Figure 4. Geometry and dimensions (mm) of (a) smooth and (b) notched (Kt=4.25) tensile specimens

The ultimate tensile fracture stress (σ_u) for both kinds of specimens was determined as the maximum load divided by the initial minimum cross section area. The extent of hydrogen embrittlement was assessed by means of the embrittlement index (EI), defined in equation 12. An EI of 100% corresponds to the maximum hydrogen embrittlement, while EI=0 means no embrittlement at all.

$$EI\ [\%] = \frac{X - X_H}{X} \cdot 100 \qquad (12)$$

Where X and X_H are the evaluated material property measured without and with hydrogen respectively.

2.9 FEM simulations

FEM Abaqus CAE software was used to obtain the stress distribution along the radius in the notch region of the tensile specimens. A 2D elastic-plastic finite element model with a Hollomon hardening law obtained from the tensile tests was developed, taking into account the axisymmetric nature of the specimens (Figure 4b). The geometry of the specimens was unevenly meshed, being this mesh finer in the vicinity of the notch root. 8-node biquadratic axisymmetric quadrilateral elements with reduced integration (CAX8R) were used with a minimum size around 40 nm. This model was also employed to determine the aforementioned K_t concentration factor.

The distribution of the normal stress perpendicular to the notch plane, σ_{22}, the Von Mises stress, σ_{VM} (equation 13), and the hydrostatic stress, σ_H (equation 14), was calculated at the moment of the failure of the specimen. The following exspressions were used.

$$\sigma_{VM} = \sqrt{\frac{(\sigma_{11}-\sigma_{22})^2+(\sigma_{22}-\sigma_{33})^2+(\sigma_{33}-\sigma_{11})^2}{2}} \qquad (13)$$

$$\sigma_H = \frac{\sigma_{11}+\sigma_{22}+\sigma_{33}}{3} \qquad (14)$$

Where σ_{11}, σ_{22} and σ_{33} are the principal stresses.

3 Results

3.1 Steel microstructure, dislocation density and residual stresses

The resultant microstructures, the dislocation density (ρ) and the residual stresses (σ_{Res}) of the 2.25Cr1Mo and 2.25Cr1MoV steels after the heat treatments described in Table 3 are respectively shown in Figure 5 and Table 5.

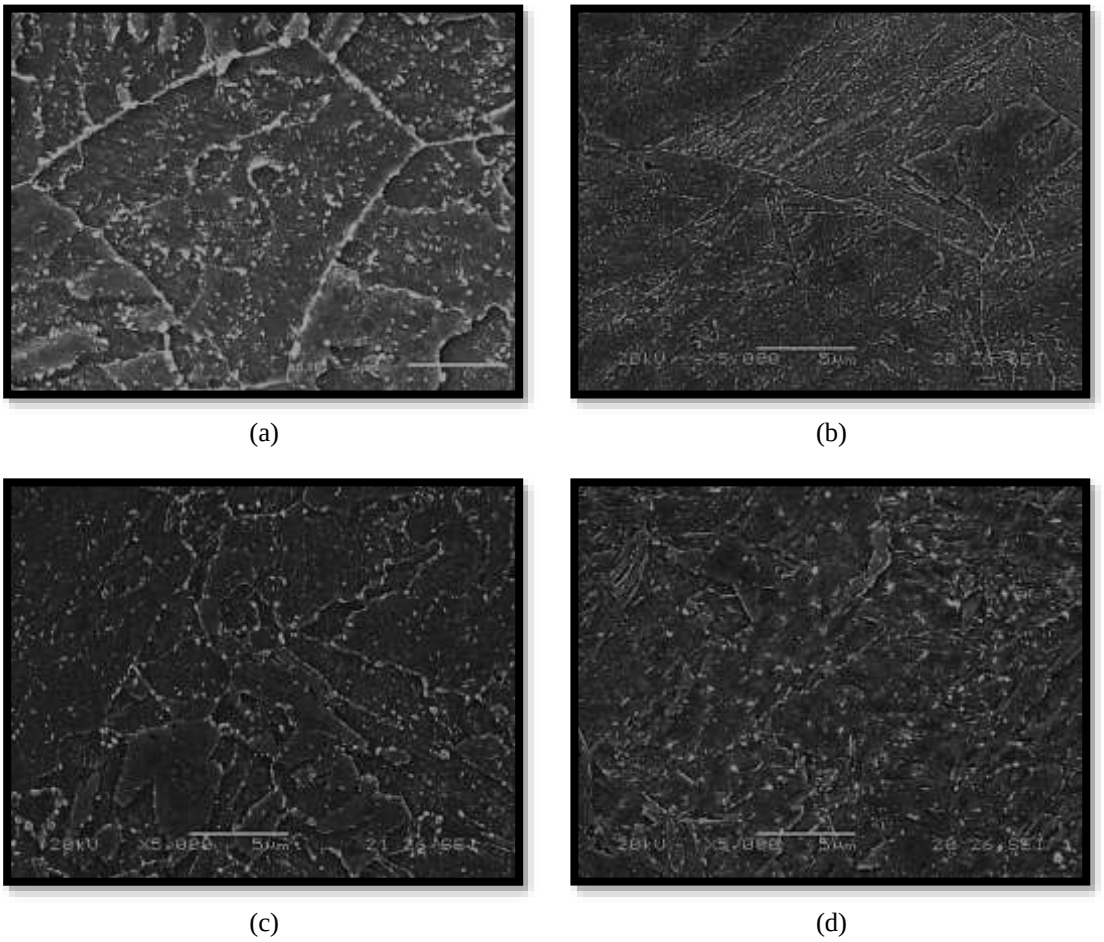

(a) (b)

(c) (d)

Figure 5. Microstructure of heat treated steels (x5000). (a) 2.25Cr1Mo_690. (b) 2.25Cr1Mo_600. (c) 2.25Cr1MoV_720. (d) 2.25Cr1MoV_650

Steel grade	$FWHM_{corrected}$ (rad)			2ε	R^2	ρ (1/cm^2)	σ_{Res} (MPa) in $\{211\}_{156.4^\circ}$
	$\{211\}_{156.4^\circ}$	$\{200\}_{106.1^\circ}$	$\{110\}_{69^\circ}$				
2.25Cr1Mo_690	0.0265	0.0090	0.0060	0.0012	0.82	$8.3\cdot10^{9}$	-18 ± 5
2.25Cr1Mo_600	0.0460	0.0110	0.0057	0.0113	0.97	$7.4\cdot10^{11}$	-90 ± 12
2.25Cr1MoV_720	0.0311	0.0100	0.0060	0.0035	0.96	$7.1\cdot10^{10}$	52 ± 12
2.25Cr1MoV_650	0.0440	0.0130	0.0070	0.0079	0.99	$3.6\cdot10^{11}$	-118 ± 10

Table 5. Dislocation density (ρ) and residual stresses (σ_{res}) of 2.25Cr1Mo(V) steel grades

Figure 6 displays the fitting of the Williamson-Hall equation, equation 2, used to determine the dislocation density of the steels. The high determination coefficient (R^2) obtained in all cases must be highlighted. It is worth noting that increasing the tempering temperature, dislocation density significantly decreases in both steels.

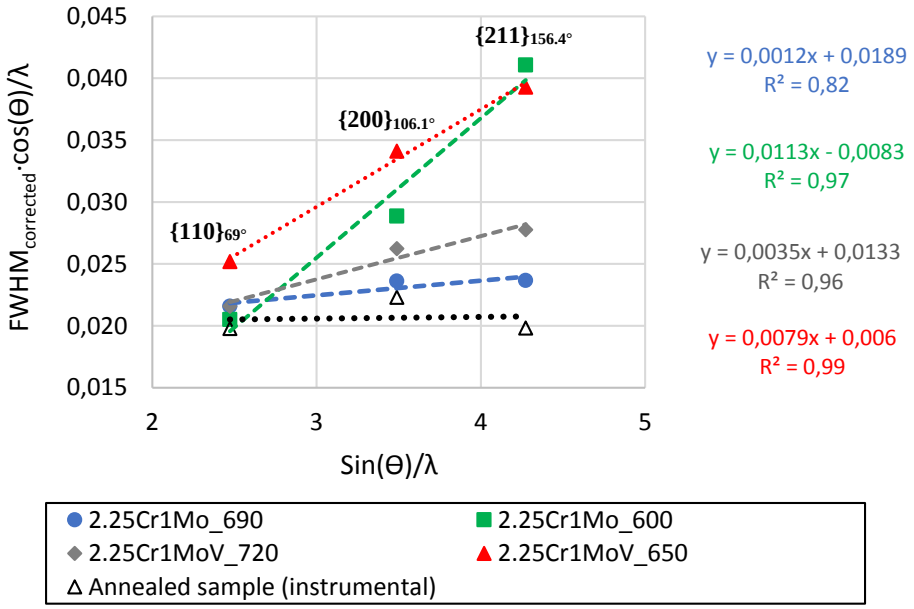

Figure 6. Dislocation density determination using the Williamson-Hall method

Regarding the microstructures showed in Figure 5, they correspond to tempered martensite in all cases, with a prior austenite grain size around 25 µm. The profuse carbide precipitation that takes place during the tempering stage is clearly seen. In the case of the 2.25Cr1Mo steel, these precipitates were identified as M_3C, $M_{23}C_6$ and M_7C_3 [42], while in the 2.25Cr1MoV steel, precipitates have been recognized as MC and M_7C_3 [43]. With increasing tempering temperature, internal residual stresses are released, dislocation rearrangement/annihilation and substructure recovery takes place (see Table 5), decreasing the interfaces between martensite lath/packet boundaries and dislocation density [44].

Microstructural differences among the studied steel grades explain the hardness (Brinell hardness) and tensile properties shown in Table 6 (σ_y: yield strength, σ_u: ultimate tensile strength, e: total elongation and RA: reduction in area). In the same table, K and n coeffcients derived from the Hollomon´s law are also shown, being σ_v the true stress and ε_{pv} the true plastic strain.

Steel grade	HB	σ_y [MPa]	σ_u [MPa]	e [%]	RA [%]	Hollomon´s law: $\sigma_v=K\cdot\varepsilon_{pv}^n$	
						K [MPa]	n
2.25Cr1Mo_690	170	430	580	27.0	80	862	0.12
2.25Cr1Mo_600	285	761	895	21.0	71	1120	0.06
2.25Cr1MoV_720	200	567	714	23.0	77	932	0.08
2.25Cr1MoV_650	262	667	829	19.0	73	1066	0.07

Table 6. Brinell Hardness (HB), tensile properties and Hollomon parameters (K and n) of the different steel grades

According to Table 6, as tempering temperature increases, the hardness and strength level decreases, while elongation and reduction in area increases in both steels. Figure 7a gives the relationship found between dislocation density (ρ) and Brinell hardness (HB). Hardness of the 2.25Cr1MoV grades are something higher than expected and this point can be explained due to hardening provided by VC precipitation in the course of tempering. Figure 7b also shows an excellent correlation between the yield strength and hardness.

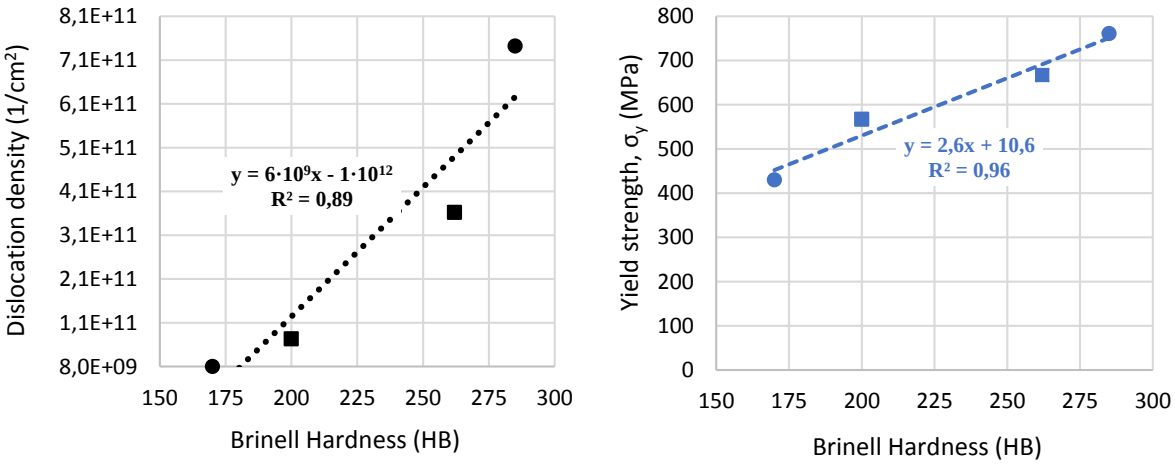

Figure 7. (a) Dislocation density versus Brinell hardness and (b) yield strength versus Brinell Hardness. 2.25Cr1Mo(V) steel grades. Circles represent V-free grades and squares represent V-added grades

Finally, in order to compare the steel grades with and without vanadium treated under the different tempering temperatures, the Hollomon-Jaffe parameter [45], exposed in equation 15 was used. The obtained results are displayed in Figure 8, where the hardening effect due to the precipitation of vanadium carbide can be appreciated.

$$P = T\,(20 + \log t) \qquad (15)$$

Where, T is the tempering temperature (in K) and t is the tempering time (in hours).

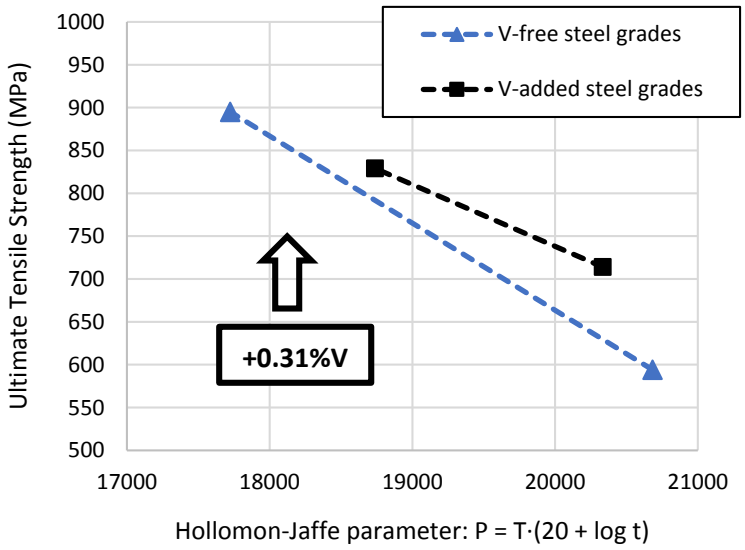

Figure 8. Ultimate tensile strength (σ_u) as a function of the tempering parameter

3.2 Hydrogen contents and hydrogen desorption curves

The hydrogen desorption curves measured at room temperature in each steel grade are shown in Figure 9. These figures represent the hydrogen content evolution (in ppm) versus the exposure time (in hours) at room temperature (RT). The hydrogen content measured in these steel grades before pre-charging was around 0.1 ppm. After hydrogen pre-charging, an initial hydrogen content (C_{H0}) of 0.6 and 1.3 ppm was measured respectively in the 2.25Cr1Mo_690 and 2.25Cr1Mo_600 grades, while in the V-added

2.25Cr1Mo steel grades, the measured initial hydrogen content was around 4 ppm. Applying Fick´s diffusion law in the radial direction of the axisymmetric cylindrical sample with a finite element model (FEM analysis) and fitting the numerical and the experimental results, the apparent diffusion coefficient (D_{app}) was obtained [46].

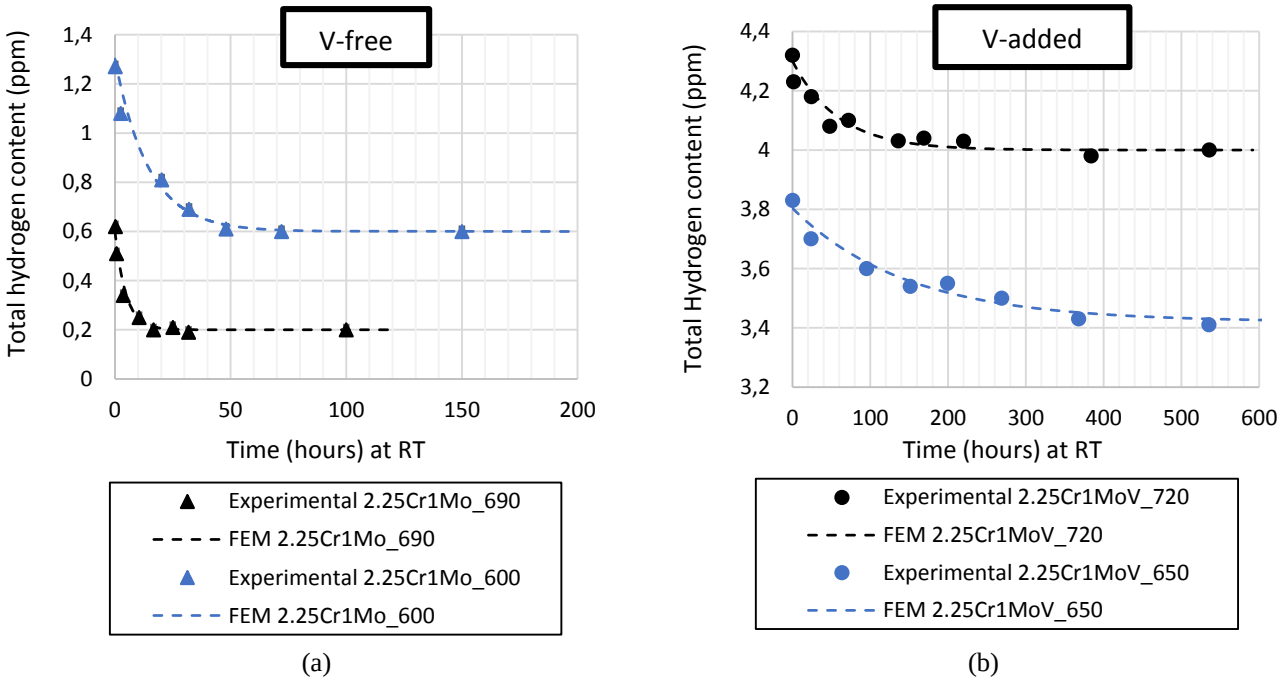

(a) (b)

Figure 9. Hydrogen desorption curves at room temperature (RT). (a) 2.25Cr1Mo steel grades (V-free) and (b) 2.25Cr1MoV steel grades (V-added)

According to Figure 9, the initial hydrogen content of each steel grade, C_{H0}, corresponds to the first point of the curve (t=0). The residual hydrogen, C_{Hf}, is the hydrogen strongly trapped in the steel microstructure, hydrogen content after a long exposure at room temperature, being the diffusible hydrogen (C_{H0} - C_{Hf}) the amount that is able to get out from traps and diffuse out of the steel in long terms. These parameters and the apparent diffusion coefficient are summarized in Table 7.

Steel grade	C_{H0} [ppm]	C_{Hf} [ppm]	C_{H0}-C_{Hf} [ppm]	C_{H0}-C_{Hf} [%]	D_{app} [m^2/s]
2.25Cr1Mo_690	0.6	0.2	0.4	68 (after 17 h at RT)	$2.5 \cdot 10^{-10}$
2.25Cr1Mo_600	1.3	0.6	0.7	53 (after 48 h at RT)	$8.0 \cdot 10^{-11}$
2.25Cr1MoV_720	4.3	4.0	0.3	9 (after 220 h at RT)	$2.0 \cdot 10^{-11}$
2.25Cr1MoV_650	3.8	3.4	0.4	11 (after 368 h at RT)	$8.0 \cdot 10^{-12}$

Table 7. Initial (C_{H0}), residual (C_{Hf}), diffusible (C_{H0}-C_{Hf}) hydrogen contents and the apparent diffusion coefficient (D_{app}) calculated from FEM analysis [46]

In the V-free steels, as tempering temperature increases, the initial and residual hydrogen contents decrease and the apparent diffusion coefficient increases, as this microstructure has the lowest density of total hydrogen traps and strong traps, mainly due to stress relaxation, reduction in dislocation density (see Table 5) and internal interfaces (martensite laths, blocks and packets). On the other hand, V-free 2.25Cr1Mo grades always desorbed hydrogen much faster than V-added grades giving rise to larger apparent diffusion coefficients (Table 7). This fact suggests that vanadium carbides (it is the main structural difference between these two steels) are very strong hydrogen-trapping sites. In the V-added grades, most hydrogen does not diffuse out from the cylidrincal samples after a long exposure time at RT (only about 10%) despite their very high initial hydrogen concentration (C_{H0}).

In order to support these results, trap hydrogen activation energies (E_a) were calculated on each steel grade and electrochemical hydrogen permeation tests were also employeed to determine the density of hydrogen traps (N_T).

3.3 Activation energy of hydrogen traps

Figure 10 gives the results of the hydrogen thermal desorption analysis (TDA) performed on the studied steel grades under different heating rates (ϕ_i), in which different hydrogen peaks were detected at specific tempertures, T_{p_i}.

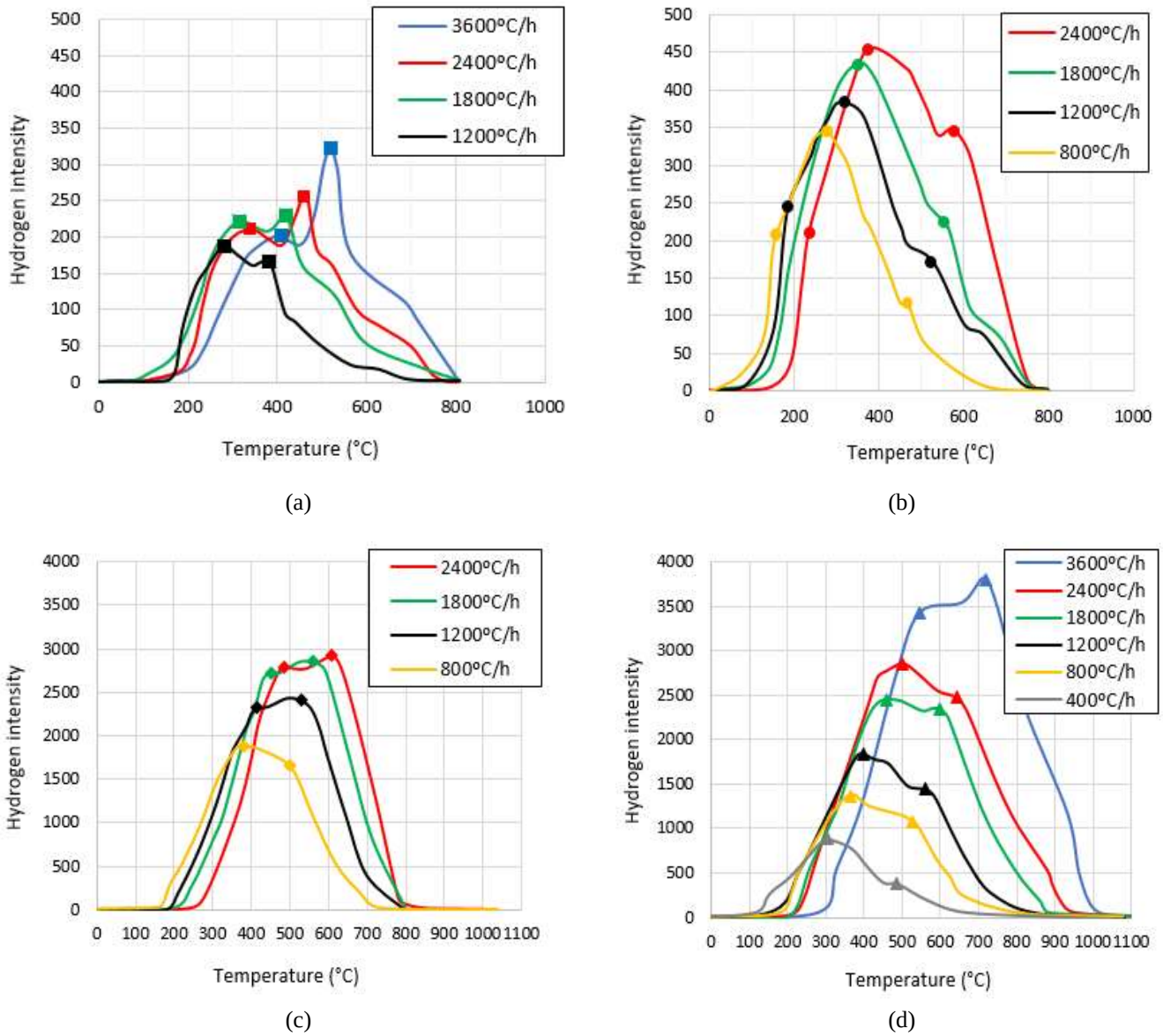

Figure 10. Thermal desorption analysis of (a) 2.25Cr1Mo_690, (b) 2.25Cr1Mo_600, (c) 2.25Cr1MoV_720 and (d) 2.25Cr1MoV_650 steel grades under different heating rates, ϕ_i(°C/h)

Figure 11 shows the different linear regressions (equation 7) applied to determine the trap activation energies corresponding to the different peaks identified in the V-free grades (a) and also in the V-added grades (b). It is worth noting the excellent fitting of these results, with R^2 determination coefficients very close to unity.

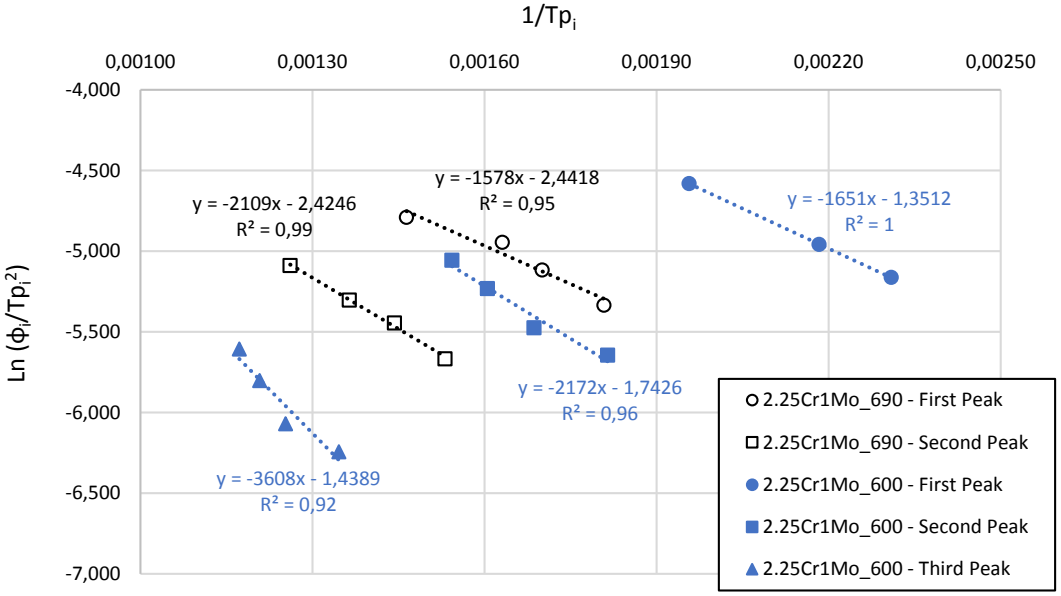

(a)

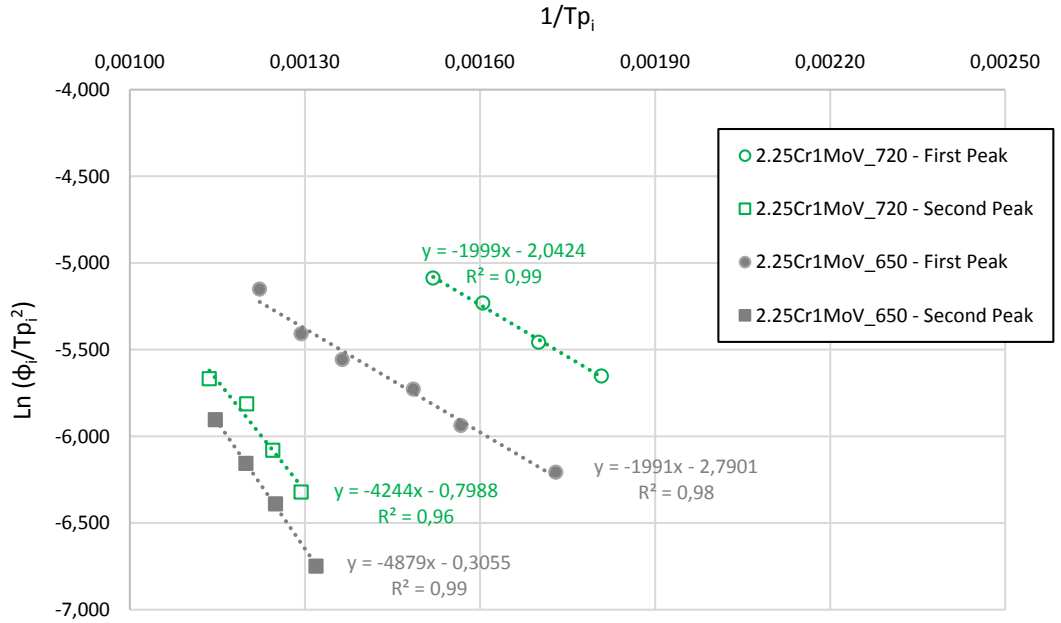

(b)

Figure 11. Determination of trap activation energies. (a) V-free steel grades. (b) V-added steel grades

Table 8 shows the slope, *m*, of the $\ln(\phi_i/T_{p_i}^2)$ versus $(1/T_{p_i})$ plots, the R^2 determination coefficient and the activation energy corresponding to the different hydrogen peaks, E_a, calculated from TDA analysis.

Grado de acero	Position peak	m (slope)	E_a [kJ/mol]	R^2
2.25Cr1Mo_690	1st	1578	13	0.95
	2nd	2109	18	0.99
2.25Cr1Mo_600	1st	1651	14	1.00
	2nd	2172	18	0.96
	3rd	3608	30	0.92
2.25Cr1MoV_720	1st	1999	17	0.99
	2nd	4244	35	0.96
2.25Cr1MoV_650	1st	1991	17	0.98
	2nd	4879	41	0.99

Table 8. Trap activation energies determined in the studied steel grades

Two peaks were identified in the 2.25Cr1Mo_690 grade tempered at 690ºC for 30 hours. The activation energy determined for the first peak, 13 kJ/mol, is in general associated with the ferrite/carbides interfaces [47-49], while the activation energy obtained for the second peak, 18 kJ/mol, was attributed to interfaces between martensite laths and packets [48-50]. On the other hand, in the grade tempered at the lowest temperature (2.25Cr1Mo_600), a third peak was found with an activation energy around 30 kJ/mol, and this energy is normally attributed to the interaction of hydrogen atoms with the elastic field of dislocations [15-18]. It is worth noting that this third peak was not observed in the 2.25Cr1Mo_690 grade, as the high tempering temperature (690ºC) has decreased the density of dislocations by a factor close to 100 (see Table 5).

Regarding the V-added grades, all the identified peaks were shifted to higher temperatures, as can be seen in Figure 10, when camparison is made for the same heating rate. This phenomenon was also observed by other authors [51]. Two peaks were always noticed in the V-added grades, the first one, with an activation energy of 17 kJ/mol, very similar to that previously calculated for the second peak in the V-free steels (see Table 8). On the other hand, a second peak with activation energies of 35 kJ/mol and 41 kJ/mol, were found in the V-added grades respectively tempered at 720ºC and 650ºC. These energies were considered to be the activation energy of hydrogen desorption from V-carbides precipitated in dislocations, and agreed well with the works of Asahi et al. [11] and Yamasaki et al. [12].

Accordingly, the higher activation energies (35-41 kJ/mol) determined in the V-added steel grades also confirm the RT desorption results given in Table 7, which showed that V-added grades present a much stronger hydrogen trapping capability and this result is explained by the presence of submicrometric vanadium carbides precipitated during the tempering treatment.

3.4 Electrochemical hydrogen permeation

Figure 12 displays the electrochemical hydrogen permeation curves obtained with the different steel grades, with and without vanadium. Table 9 summarizes the parameters obtained from the mentioned permeation curves and Figure 13 gives as an example the theoretical data adjustment ($1 \geq J/J_{max} \geq 0.9$) performed to estimate the lattice diffusion coefficient in the case of the 2.25Cr1Mo_690 steel grade.

According to the results shown in Table 9 and regarding the V-free grades, 2.25Cr1Mo_600, with a lower tempering temperature, has a trapping density (N_T) around two orders of magnitude higher than 2.25Cr1Mo_690 (higher tempering temperature) and, consequently, the apparent diffusion coefficient (D_{app}) determined in the 2.25Cr1Mo_600 grade was eight times lower than the one estimated for the grade tempered at the highest temperature. Moreover, it is also worth noting that the apparent hydrogen concentration, C_{app}, in the 2.25Cr1Mo_600 is strongly increased due to higher trapping.

Regarding the V-added steel grades, a similar effect was noticed. As tempering temperature decreases, the density of traps increases and then, the apparent diffusion coefficient decreases, while the apparent hydrogen concentration increases.

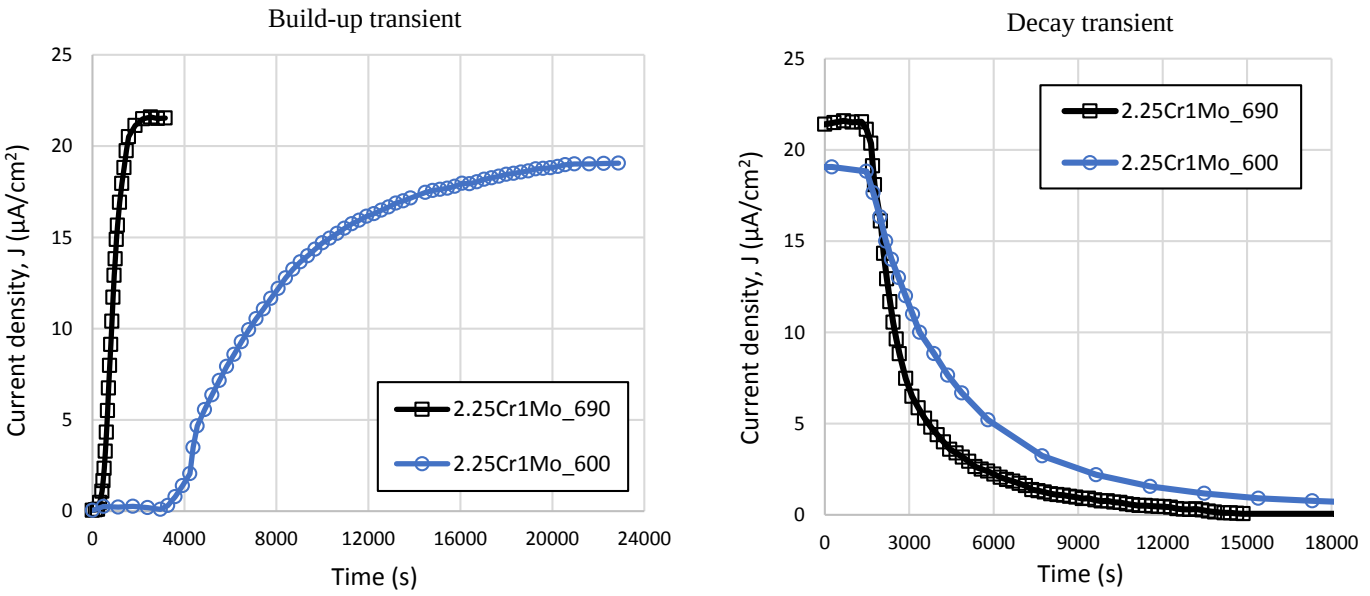

(a)

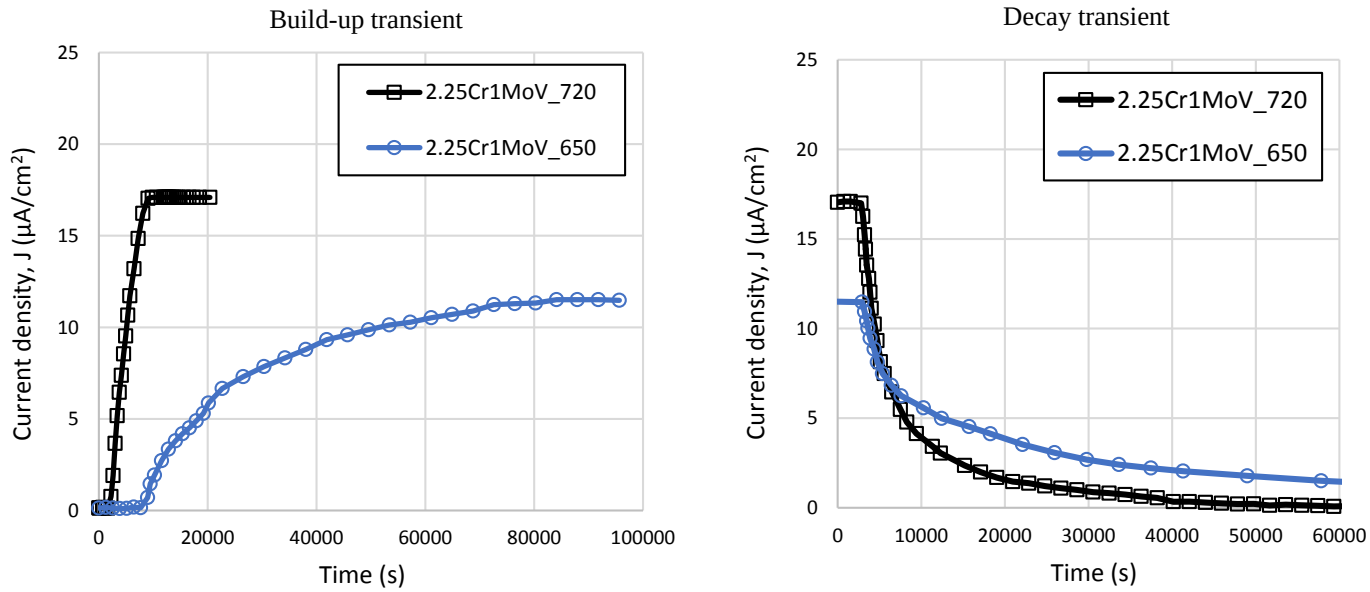

(b)

Figure 12. Hydrogen permeation curves (under 1 mA/cm^2). (a) V-free steels and (b) V-added steels

Steel grade	J_{max} [μA/cm^2]	C_{app} [ppm]	D_{app} [m^2/s]	$D_{Lattice}$ [m^2/s]	N_T [sites/m^3]
2.25Cr1Mo_690	21.5	1.7	$1.7 \cdot 10^{-10}$	$3.0 \cdot 10^{-10}$	$1.1 \cdot 10^{24}$
2.25Cr1Mo_600	19.0	11.9	$2.1 \cdot 10^{-11}$	$2.5 \cdot 10^{-10}$	$1.0 \cdot 10^{26}$
2.25Cr1MoV_720	17.0	7.1	$2.6 \cdot 10^{-11}$	$1.6 \cdot 10^{-10}$	$2.3 \cdot 10^{25}$
2.25Cr1MoV_650	11.5	26.5	$5.2 \cdot 10^{-12}$	$1.1 \cdot 10^{-10}$	$4.2 \cdot 10^{26}$

Table 9. Results of hydrogen permeation tests. 2.25Cr1Mo(V) steel grades

Finally, the lattice diffusion coefficient ($D_{Lattice}$) determined with the four grades gave values in the range of 10^{-10} m^2/s, which are lower than the values of the lattice diffusivity of hydrogen in pure iron ($D_{Fe\alpha} \sim 10^{-8}$-$10^{-9}$ m^2/s) [39, 41, 52], being justified by the effect of solute atoms and by the presence of internal stresses (Table 5) [53].

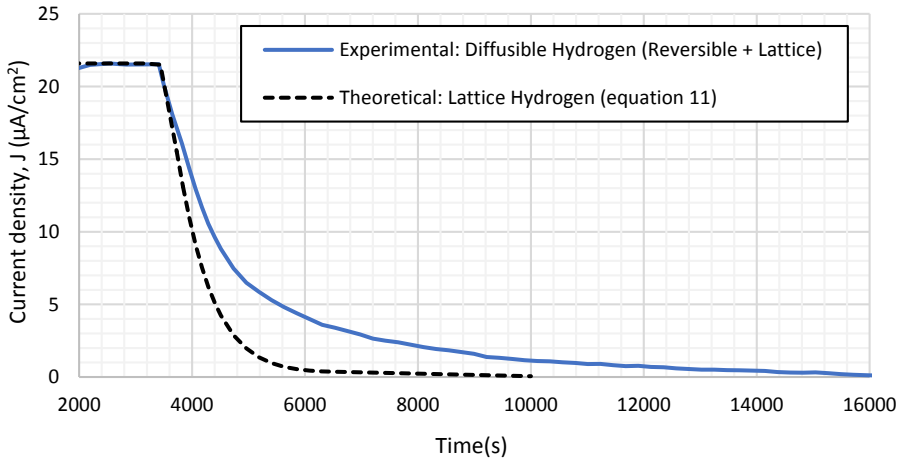

Figure 13. Decay transient (after switching-off the cathodic current). 2.5Cr1Mo_690 ($D_{Lattice}=3\cdot10^{-10}$ m^2/s in Table 9)

3.5 Tensile tests on smooth specimens

Figure 14 and Table 10 show the stress-strain curves and the tensile properties obtained for the V-free and V-added steels uncharged and hydrogen pre-charged and tested at different displacement rates.

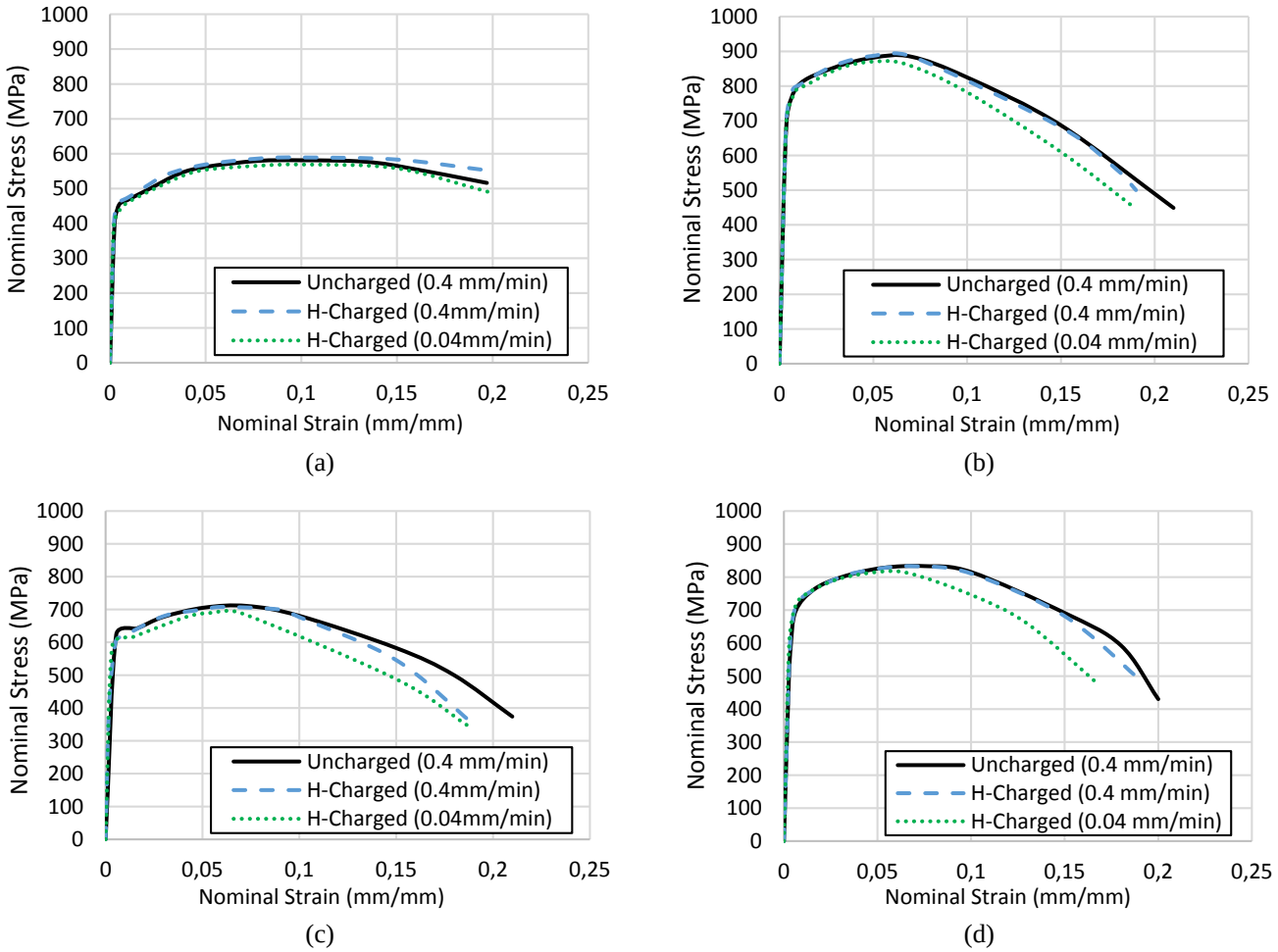

Figure 14. Stress-strain curves. (a) 2.25Cr1Mo_690, (b) 2.25Cr1Mo_600, (c) 2.25Cr1MoV_720 and (d) 2.25Cr1MoV_650

The duration of the tests and the hydrogen content at the start and at the end of the tests, C_0, C_f, estimated from the hydrogen desorption curves (Figure 9) are also given in Table 10. In the same table, the embrittlement indexes (EI) corresponding to yield strength (σ_y), ultimate tensile strength (σ_u), elongation (e) and reduction in area (RA) are also shown.

Steel grade	Displacement rate (mm/min)	Test duration (min)	σ_y (MPa)	σ_u (MPa)	e (%)	RA (%)	EI (%)				$C_o \rightarrow C_f$ (ppm)
							σ_y	σ_u	e	RA	
2.25Cr1Mo_690	0.4	16	430	580	27.0	80	-	-	-	-	Uncharged
	0.4	18	450	590	27.0	78	0	0	0	3	0.60 → 0.57
	0.04	183	430	570	26.0	77	0	2	4	4	0.60 → 0.26
2.25Cr1Mo_600	0.4	12	761	895	21.0	71	-	-	-	-	Uncharged
	0.4	14	776	897	17.0	68	0	0	19	4	1.30 → 1.30
	0.04	126	757	882	16.0	63	1	1	24	11	1.30 → 0.96
2.25Cr1MoV_720	0.4	10	567	714	23.0	77	-	-	-	-	Uncharged
	0.4	15	580	717	21.0	75	0	0	9	3	4.30 → 4.30
	0.04	137	600	706	19.5	73	0	1	15	5	4.30 → 4.30
2.25Cr1MoV_650	0.4	18	667	829	19.0	73	-	-	-	-	Uncharged
	0.4	15	685	833	17.0	70	0	0	11	4	3.80 → 3.80
	0.04	140	685	817	15.0	68	0	1	21	7	3.80 → 3.80

Table 10. Tensile results on smooth specimens, embrittlement indexes and hydrogen evolution estimation during the tests

Tensile properties of hydrogen pre-charged smooth specimens remained barely unaffected independently of the applied displacement rate. Embrittlement indexes calculated on the different grades were quite low although it is worth noting that grades submitted to lower tempering temperature were slightly more sensitive to hydrogen embrittlement (hardest grades, 2.25Cr1Mo_600 and 2.25Cr1MoV_650) and such sensitivity increased when tested at the lowest displamente rates. Regarding the failure micromechanism, the typical ductile fracture mechanism, which consists on nucleation, growth and coalescence of microvoids, was observed on the uncharged and also on all the pre-charged specimens under the scanning electron microscope. This fact may be related to the low triaxiality of the smooth tensile specimens, that precludes hydrogen accumulation accoding to the Oriani theory (equation 1).

3.6 Tensile tests on notched specimens

3.6.1 Experimental results

Figure 15 gives the stress-strain curves of the uncharged and hydrogen pre-charged notched specimens. Tensile tests curves performed on notched specimen show a reduced plastic region, as most of the specimen is only elastically strained, except a very small region close to the stress concentrator (notch tip region).

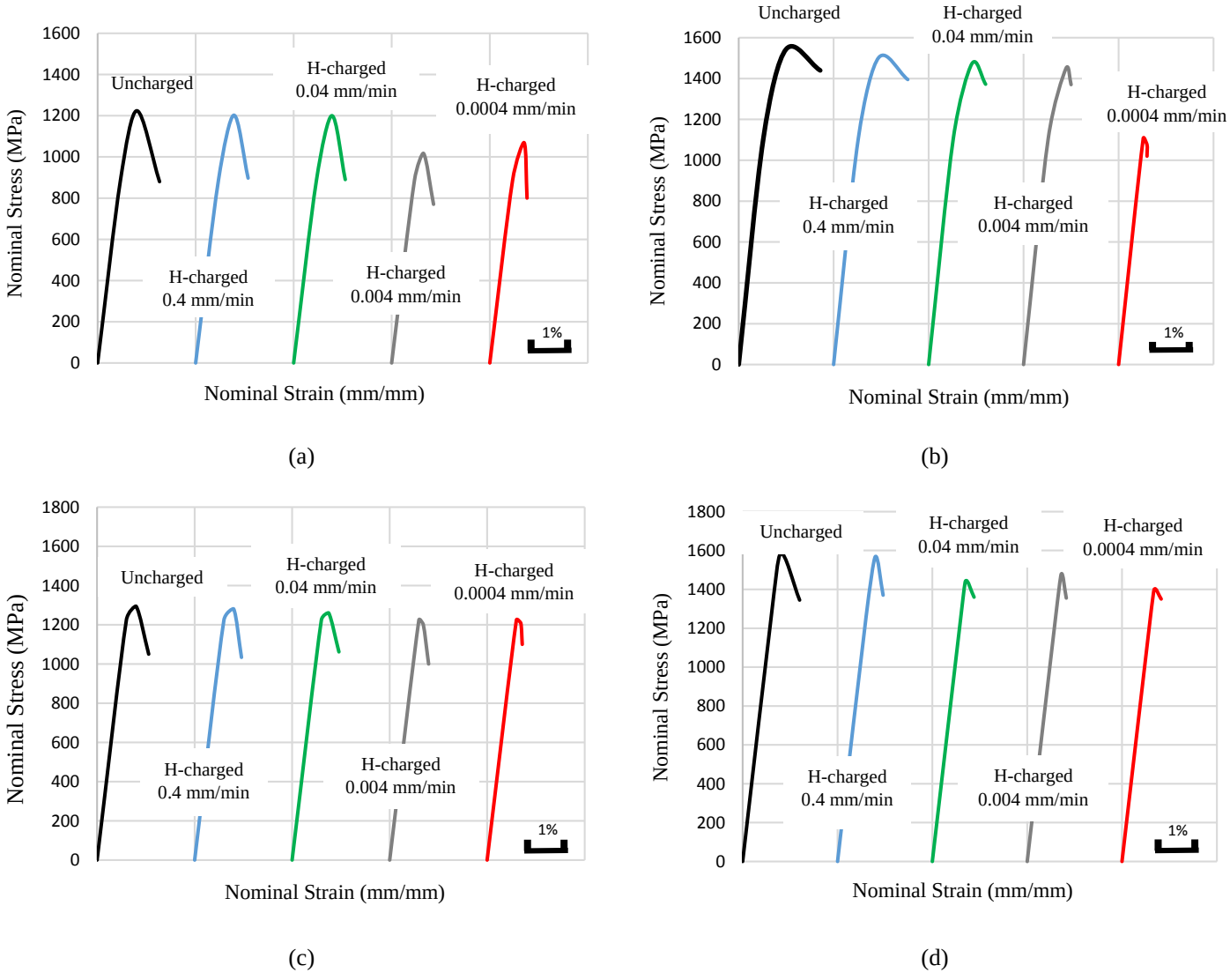

Figure 15. Stress-strain curves in notched tensile tests (a) 2.25Cr1Mo_690, (b) 2.25Cr1Mo_600, c) 2.25Cr1MoV_720 and d) 2.25Cr1MoV_650

Table 11 shows the results obtained under the different applied displacement rates, from 0.4 to 0.0004 mm/min: as the test displacement rate decreases, hydrogen embrittlement increases, being this effect more notable in the grades tempered at the lowest temperatures.

Steel grade	Displacement rate (mm/min)	Test duration	σ_u (MPa)	RA (%)	EI (%)		$C_o \rightarrow C_f$ (ppm)	*Fracture Micromechanisms
					σ_u	RA		
2.25Cr1Mo_690 (σ_y=430 MPa)	0.4	10 min	1224	20.5	-	-	Uncharged	MVC
	0.4	10 min	1202	18.9	0	8	0.60 → 0.60	MVC
	0.04	80 min	1200	17.4	2	15	0.60 → 0.36	MVC
	0.004	13 hours	1017	13.0	17	37	0.60 → 0.20	MVC+PRHIC
	0.0004	5 days	1069	9.0	13	56	0.60 → 0.20	MVC+PRHIC
2.25Cr1Mo_600 (σ_y=761 MPa)	0.4	10 min	1533	17.0	-	-	Uncharged	MVC
	0.4	15 min	1503	16.0	2	6	1.30 → 1.28	MVC
	0.04	127 min	1479	7.0	3.5	59	1.30 → 0.95	MVC
	0.004	10 hours	1448	4.0	5.5	76	1.30 → 0.65	MVC+cleavages+PRHIC+IG
	0.0004	4 days	1076	3.0	30	82	1.30 → 0.60	Cleavages+PRHIC+IG
2.25Cr1MoV_720 (σ_y=567 MPa)	0.4	10 min	1294	18.0	-	-	Uncharged	MVC
	0.4	10 min	1281	17.5	1	3	4.30 → 4.32	MVC
	0.04	90 min	1261	14.0	3	22	4.30 → 4.29	MVC
	0.004	15 hours	1202	12.0	7	33	4.30 → 4.20	MVC
	0.0004	4 days	1209	9.0	5	50	4.30 → 4.04	MVC
2.25Cr1MoV_650 (σ_y=667 MPa)	0.4	10 min	1585	16.5	-	-	Uncharged	MVC
	0.4	10 min	1568	12.0	1	28	3.80 → 3.83	MVC
	0.04	60 min	1456	9.0	9	47	3.80 → 3.81	MVC
	0.004	11 hours	1479	8.0	7	52	3.80 → 3.74	MVC
	0.0004	6 days	1400	7.0	12	60	3.80 → 3.53	MVC+cleavages+PRHIC
*MVC: microvoid coalescence, PRHIC: plasticity related hydrogen induced cracking, IG: intergranular								

Table 11. Tensile results on notched specimens, 2.25Cr1Mo(V) steels (K_t=4.25), embrittlement indexes, hydrogen evolution estimation during the tests and predominat failure micromechanisms

In the case of the V-free 2.25Cr1Mo_690 steel, the notch tensile strength with pre-charged internal hydrogen tested at the lowest displacement rate, 0.0004 mm/min, was 1069 MPa with a reduction of area of 9% (see Table 11), while this grade had shown a notched strength of 1224 MPa and a reduction of area of 20.5% in the uncharged condition, giving then rise to embittlement indexes of 13 and 56% respectively. On the other hand, the notch tensile strength of the 2.25Cr1Mo_600 grade (lower tempering temperature), under the lowest displacement rate was 1076 MPa with a reduction of area around 3% (see Table 11), while, the notch tensile strength and the reduction in area were respectively 1533 MPa and 17% in the uncharged test (embrittlement indexes of 30 and 82%).

Regarding now the V-added grades, the ultimate tensile strength was barely affected by the presence of internal hydrogen but, on the opposite, reduction in area (RA) was significantly affected, especially in tests performed under low displacement rates. The V-added steel grade tempered at 650ºC (lower tempering temperature) was more sensitive to hydrogen embrittlement. In fact, the fracture strength of this grade decreased around 12% and reduction in area around 60% (Table 11), when hydrogen pre-charged specimens were tested at the lowest displacement rate (0.0004 mm/min).

3.6.2 Finite element simulations

As it was already mentioned, hydrogen distribution in the notch region is dominated by hydrostatic stress even when plastic strain is high, in this way, low displacement rates allow hydrogen to diffuse along the steel microstructure and move to attain the stress concentration region located in front of the notch (high triaxiality). Due to the accumulation of hydrogen in this area, a critical hydrogen concentration can be reached, giving rise to a premature failure.

In order to explain the experimental results obtained with the notched specimens, the distribution of the local normal stress perpendicular to the notch plane, σ_{22}, the Von Mises stress, σ_{VM}, the hydrostatic stress, σ_H, and also the σ_{VM}/σ_y ratio were calculated along the radial path defined from the free surface at the tip

of the notch (x=0) to the centre of the specimen in the notched section (x=2.5 mm). The aforementioned distribution of stresses along the sample radial direction when the applied stress is equal to the notch tensile strength is given in Figure 16.

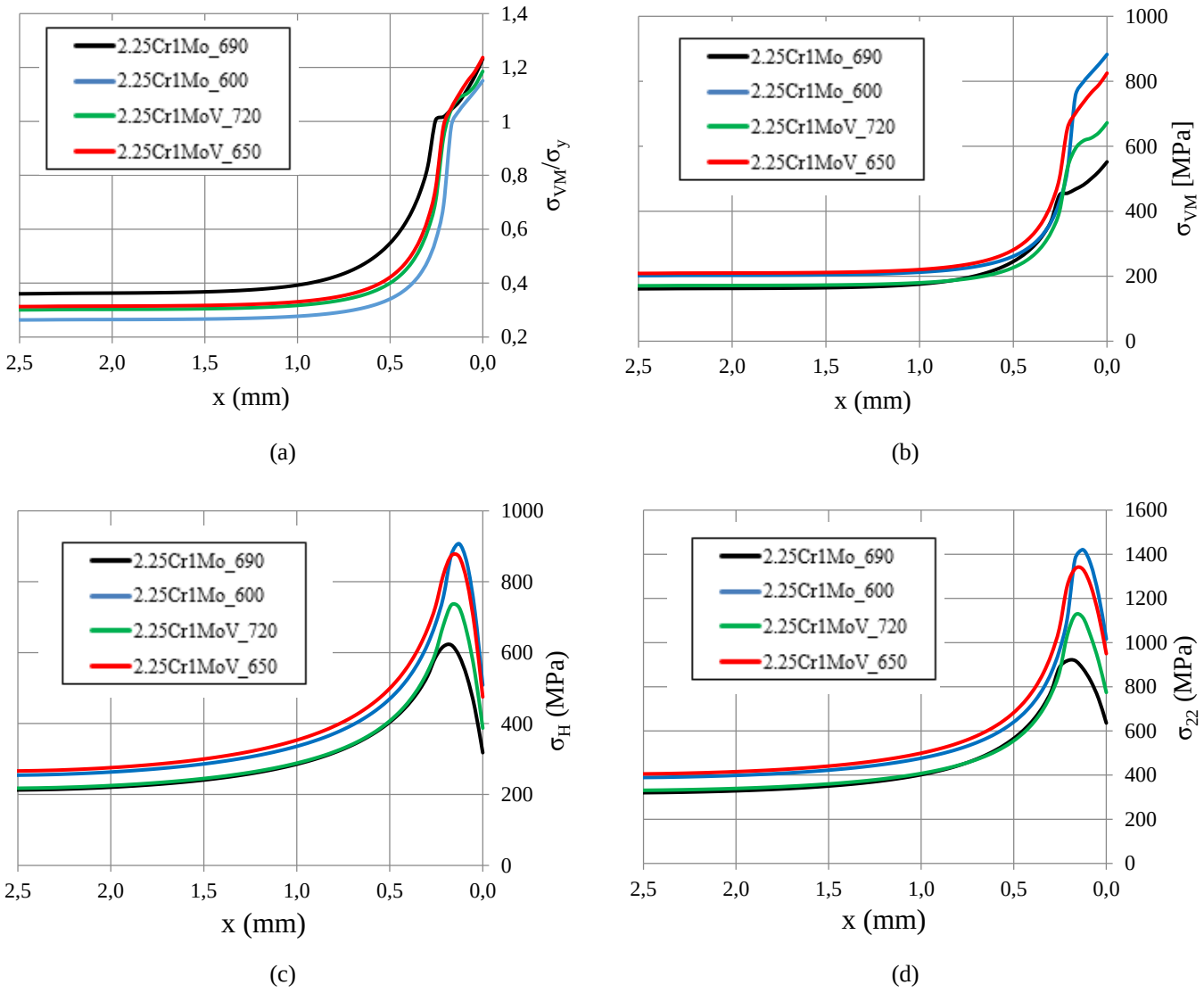

Figure 16. Distribution of (a) $\sigma_{VM}/\sigma y$, (b) σ_{VM}, (c) σ_H and (d) σ_{22} along the radial direction when the applied stress is equal to the notch tensile strength

Figure 16a shows the $\sigma_{VM}/\sigma y$ ratio versus the distance from notch tip at an applied stress equal to the notch tensile srength for the four steel grades. The extensión of the plastic zone ($\sigma_{VM}/\sigma_y = 1$) varies between 100 and 250 µm, increasing in both steels as the tempering temperature does (lower yield strength). In addition, Figure 16b, c and d show the σ_{VM}, σ_H and σ_{22} versus distance from the notch tip. The influence of the steel yield strength on the Von Mises stress level close to the notch tip is also clearly seen in Figure 16b, as such stress increases significantly as the steel yield strength increases. A peak on the hydrostatic stress (Figure 16c) and on the normal stress (Figure 16d) at a certain distance (125-250µm) from the notch tip develop in these tests with maximum values increasing as the steel yield strength does. According to equation 1, hydrogen accumulation will take place in this location.

3.6.3 Fracture surfaces

In order to complete the analysis of hydrogen effect on the degradation of the tensile properties of the steels, the fracture surfaces of the notched specimens were analysed. Figure 17 shows the surface corresponding to the uncharged 2.25Cr1Mo_690 grade, which shows a ductile micromechanism, consisting on initiation, growth and coalescence of microvoids, MVC.

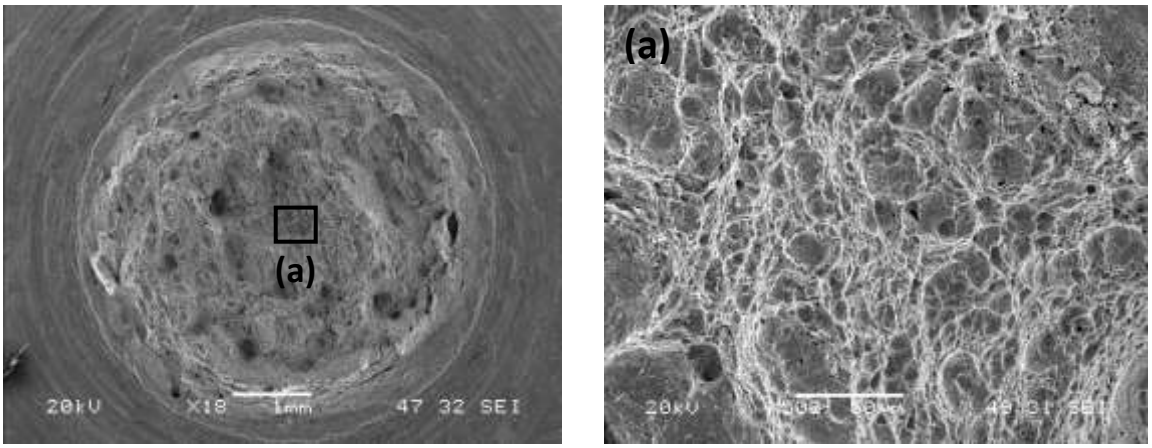

(a) General fracture surface (b) Detail region marked as (a)

Figure 17. Fracture surfaces of uncharged 2.25Cr1Mo_690 grade tested at 0.4 mm/min

Figure 18 shows now the fracture surfaces of the same steel hydrogen pre-charged and tested at the lowest displacent rate (0.0004 mm/min), where hydrogen embrittlement was maximum. The main failure micromechanism was also ductile (MVC). In the central region of the sample, quite large and flat areas are noticed (black arrows, see Figure 18b). These areas are shallow voids, which have grown due to the enhanced and localized plasticity produced by the presence of hydrogen. This failure mechanism is known as HELP (hydrogen enhanced localized plasticity). Nevertheless, the region just ahead the notch tip (first 150 µm, from the notch tip, see Figure 18c), where the hydrostatic stress attains the maximum value (σ_H ~ 600 MPa, Figure 16c), has the appearance of a transgranular fracture or quasi-cleavage (HEDE, hydrogen-enhanced decohesion), micromechanism that is usually denoted as PRHIC or plasticity related hydrogen induced cracking in quenched and tempered steels (Figure 18d).

The PRHIC mechanism was first described by Takeda and McMahon [54] in reference to the fracture mechanism observed in a low alloy quenched and tempered steel in hydrogen gas. It is described as a fracture surface characterized by ductile micro-plastic tearing on a very fine scale, along martensite lath interfaces. Hydrogen accumulation promotes plastic deformation and final fracture along these interfaces. Failure initiates just ahead of the notch under this mechanism and MVC takes place afterwards in the centre of the sample.

It is important to mention that the same micromechanisms were also observed at 0.004 mm/min (as indicated in Table 11) but in this case, PRHIC extension was something smaller. On the other hand, at 0.4 and 0.04 mm/min, PRHIC micromechanism was not noticed and the only failure micromechanism was coalescence of microvoids (MVC), see Table 11.

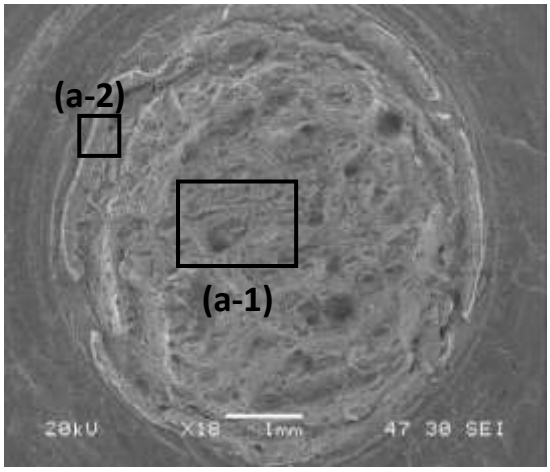

(a) General fracture surface

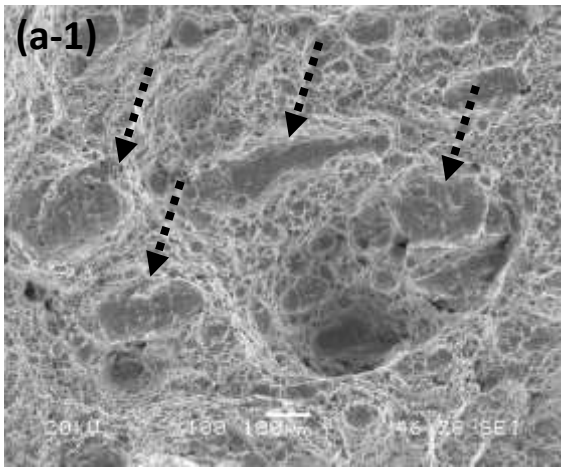

(b) Detail zone (a-1), interior

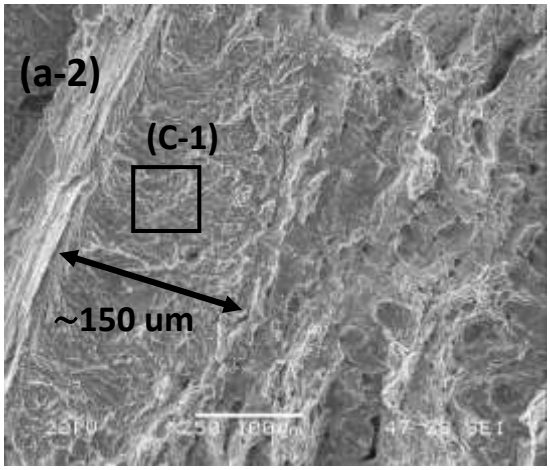

(c) Detail region (a-2), surface

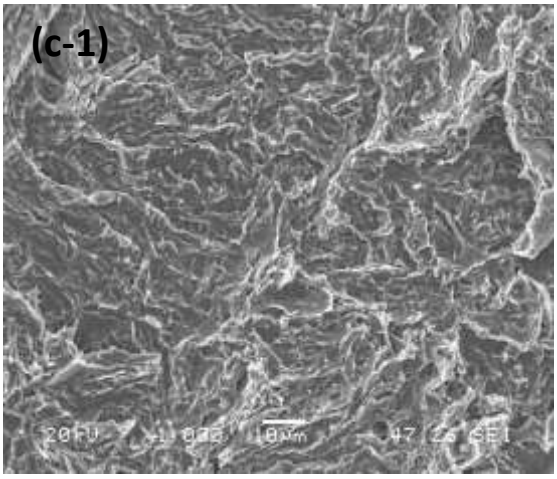

(d) Detail region (c-1)

Figure 18. Fracture surfaces corresponding to hydrogen pre-charged 2.25Cr1Mo_690 tested at 0.0004 mm/min (5 days testing), EI σ_u ~ 13% and EI RA ~ 56%

Regarding now the 2.25Cr1Mo_600 steel grade (lower tempering temperature), their fracture surfaces were shown in Figure 19 and Figure 20.

Figure 19 corresponds to the uncharged specimen and shows a ductile failure micromechanism, consisting on initiation, growth and coalescence of microvoids, similar to the one operative in the high temperature tempered grade, 2.25Cr1Mo_690.

Fracture surfaces corresponding to the hydrogen pre-charged specimens tested at the lowest displacement rate (0.0004 mm/min) are shown in Figure 20. On the general fracture surface, two different regions are noticed. The first one, located in the surface region above the dotted line marked in the figure, where failure initiated, is characterized by the presence of PRHIC and intergranular fracture (IG) micromechanisms (Figure 20b and c). This region attains a maximum depth of 1 mm corresponding to the high hydrostatic stress area (σ_H > 800 MPa, Figure 16c). Cleavage micromechanism was also present in the bulk of this specimen (Figure 20d).

The same hydrogen micromechanisms were also observed at 0.004 mm/min, where hydrogen embrittlement was also significant but, in this case, the depth of the most embrittled region also characterized by the presence of PRHIC and IG micromechanisms was lower (around 500 μm). On the contrary, under the highest displacement rates (0.4 and 0.04 mm/min), these failure micromechanisms were not observed, but only MVC (Table 11).

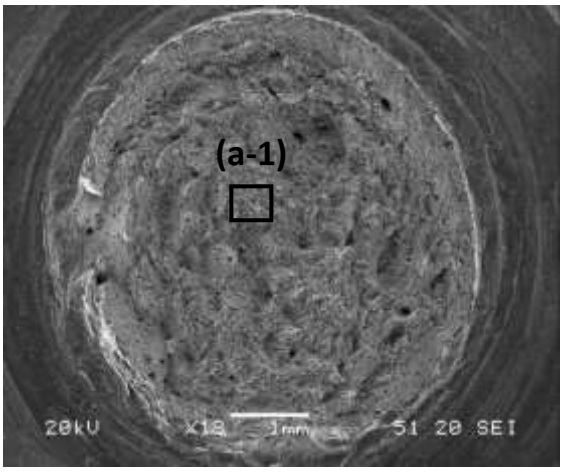

(a) General fracture surface

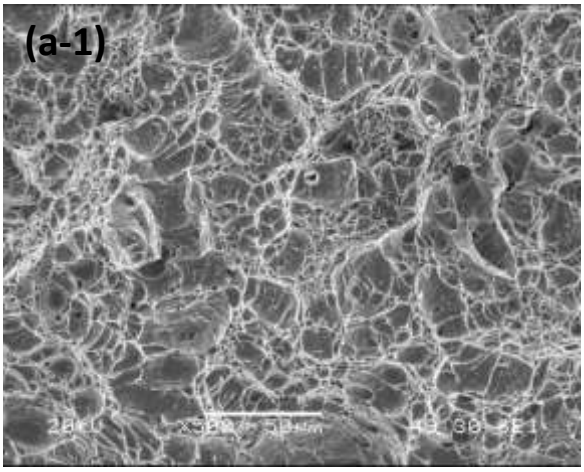

(b) Detail region marked as (a-1)

Figure 19. Fracture surfaces corresponding to the uncharged 2.25Cr1Mo_600 grade tested at 0.4 mm/min

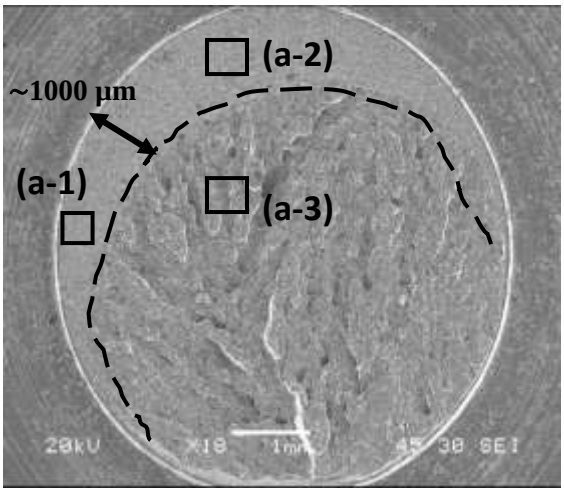

(a) General fracture

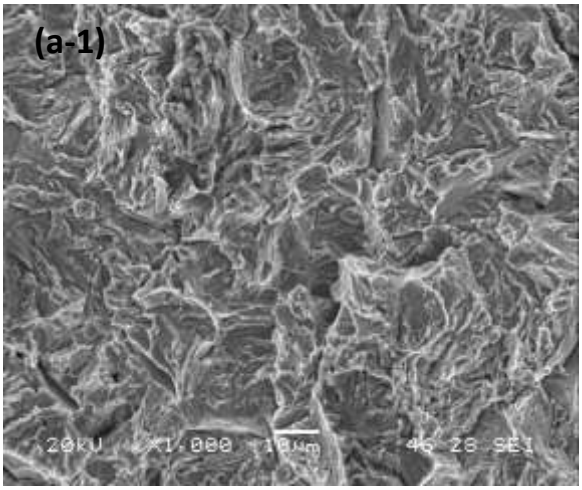

(b) Detail region a-1

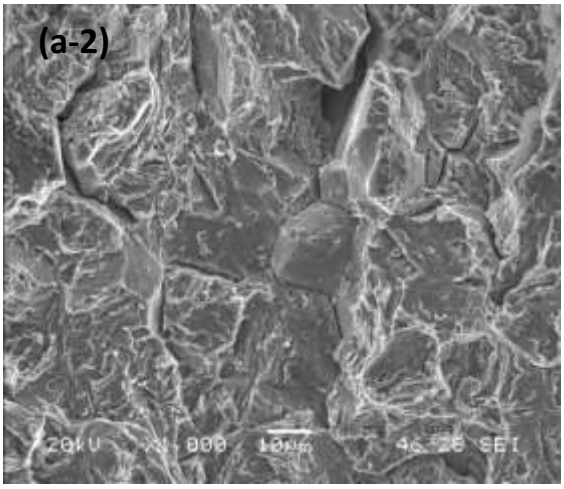

(c) Detail region a-2

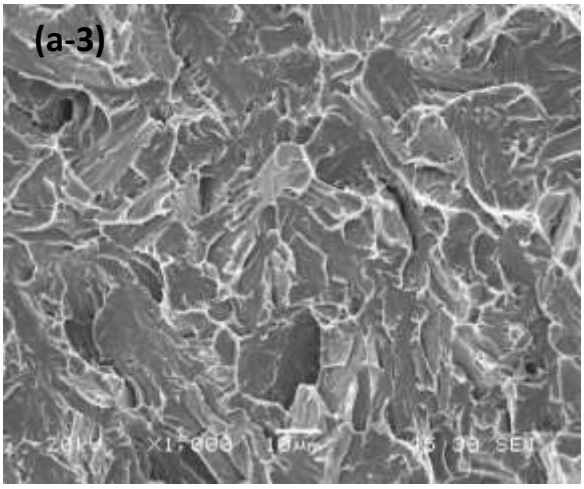

(d) Detail region a-3

Figure 20. Fracture surfaces corresponding to hydrogen pre-charged 2.25Cr1Mo_600 grade tested at 0.0004 mm/min (4 days testing), EI σ_u ~ 30% and EI RA ~ 82%

Figure 21 shows now the appearance of the failure surface of the uncharged 2.25Cr1MoV steel grades (tempered at 720ºC and 650ºC): a ductile micromechanism, consisting on initiation, growth and coalescence of microvoids (MVC) on both steel grades was observed.

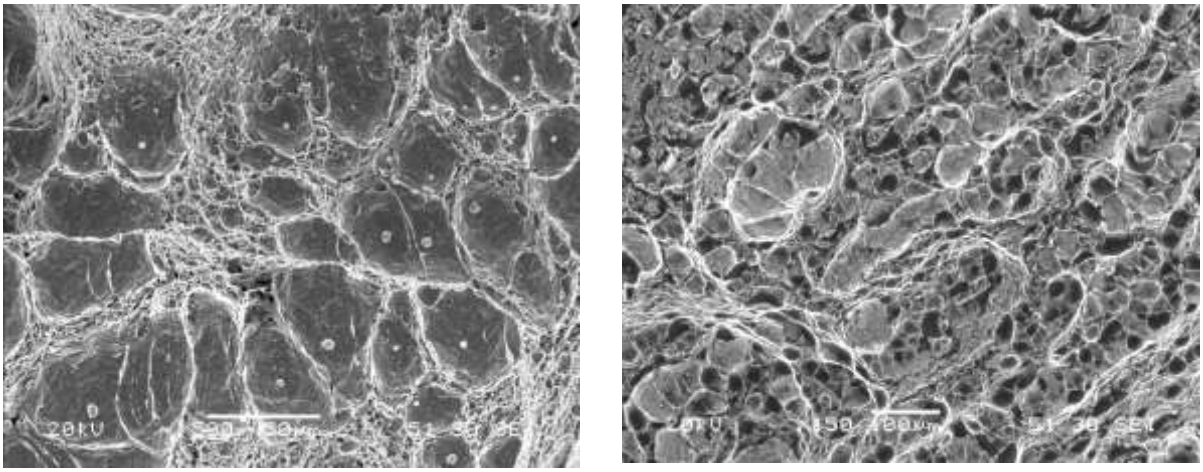

(a) (b)

Figure 21. Fracture surfaces corresponding to the uncharged 2.25Cr1MoV grades tested at 0.4 mm/min. (a) 2.25Cr1MoV_720. (b) 2.25Cr1MoV_650

On the other hand, the fracture surfaces corresponding to the hydrogen pre-charged specimen and tested at the lowest displacent rate (0.0004 mm/min) are respectively shown in Figure 22 and Figure 23 for the grade tempered at the highest (2.25Cr1MoV_720) and lowest (2.25Cr1MoV_650) temperature.

Although reduction in area and ultimate tensile strength embrittlement indexes of 50% and 5% were respectively measured in the 2.25Cr1MoV_720 grade tested at the lowest displacement rate (see Table 11), failure micromecahnisms did not change respect the uncharged condition. Only the presence of shallow voids, enlarged due to localized plasticity produced by hydrogen accumulation in the notch section (HELP mechanism) is worth mentioning, see Figure 22b.

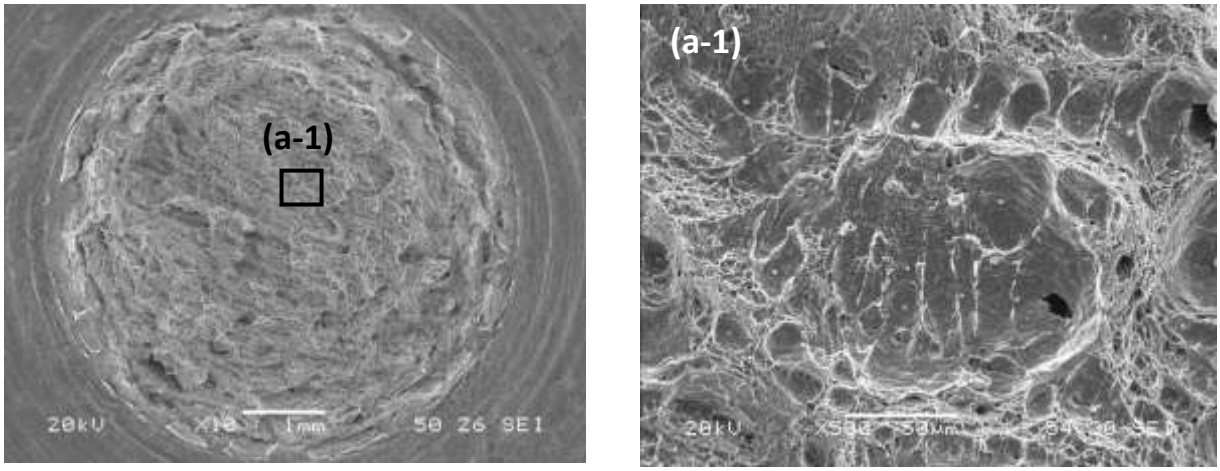

(a) General fracture (b) Detail region, marked as a-1

Figure 22. Fracture surfaces corresponding to hydrogen precharged 2.25Cr1MoV_720 tested at 0.0004 mm/min (4 days testing), EI σ_u ~ 5% and EI RA ~ 50%

Finally, the 2.25Cr1MoV_650 steel grade, tempered at a lower temperature and with a higher yield strength (reduction in area and ultimate tensile strength embrittlement indexes of 60% and 12% respectively) exhibited important changes on the fracture surface when it was tested at 0.0004 mm/min, as can be see in Figure 23. In the bulk of the specimen, MVC with enlongated voids, see Figure 23a and b, was the predominant micromechanism, although some areas with cleavages (see Figure 23c) were noticed along some radial paths leading from the periphery to the centre of the specimen. Moreover, PRHIC

micromechanism was observed until a depth of 150 μm in some regions of the specimen periphery (see Figure 23d and e), where failure initiated due to the high local hydrostatic stress, which attains values around 870 MPa in this grade, Figure 16c).

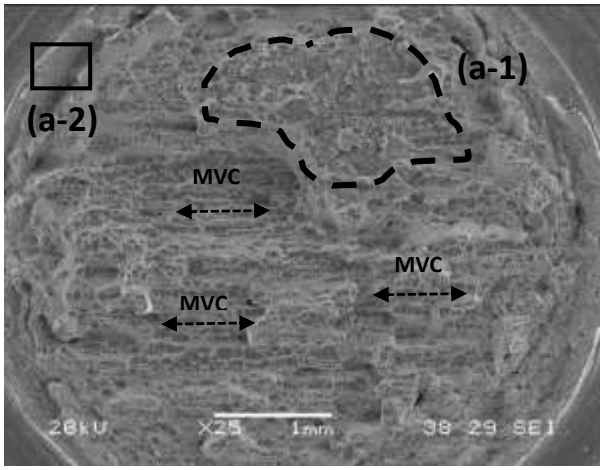

(a) General fracture surface

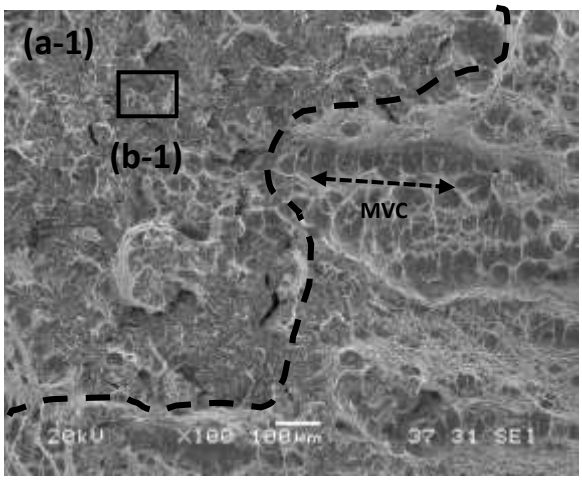

(b) Detail region marked as (a-1)

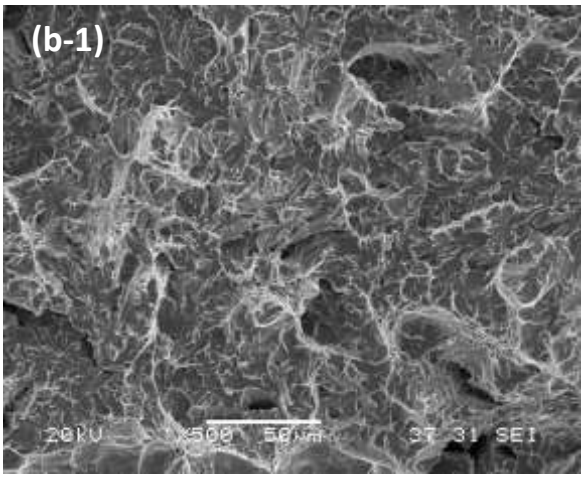

(c) Detail region marked as (b-1)

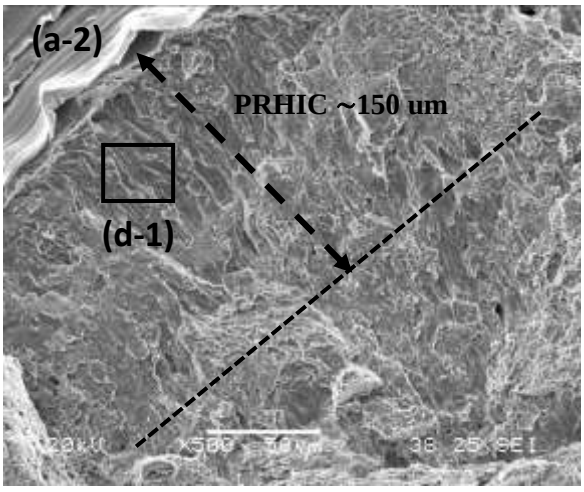

(d) Detail region marked as (a-2)

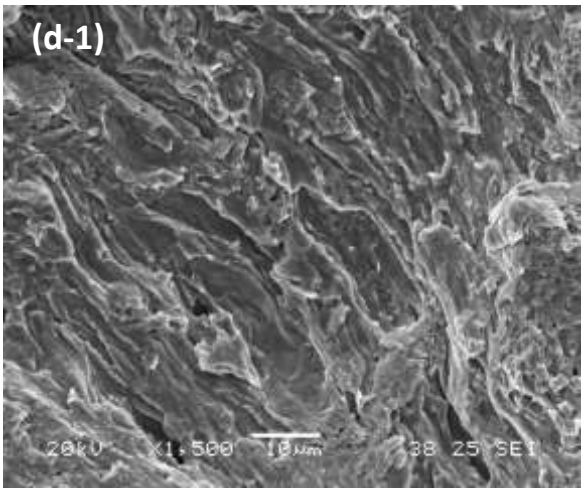

(e) Detail región marked as (d-1)

Figure 23. Fracture surfaces corresponding to hydrogen precharged 2.25Cr1MoV_650 grade tested at 0.0004 mm/min (6 days testing), EI σ_u ~ 12% and EI RA ~ 60%

4 Discussion

When a tensile load is applied to a notched specimen, hydrogen atoms located in the sorroundings on the notch will diffuse towards the notch-tip region driven by the high hydrostatic stress existing in this area. In this situation, when a critical hydrogen concentration is reached, the different hydrogen embrittlement mechanisms (HELP/HEDE) can take place, contributing to decrease the mechanical properties of the steel. Moreover, the time that hydrogen has to attaint the aforementioned region, just ahead of the notch, depends on the duration of the mechanical test (the use of low displacement rates allows more hydrogen atoms to attain the noth-tip region). Therefore, hydrogen diffusion coefficient (D_{app}) plays an important role on the embrittlement process. Accordingly, it is important to analyse the interaction of hydrogen atoms with the microstructure of the steel in order to explain the degradation of the steel tensile properties due to the presence of internal hydrogen.

In order to analyse the effect of the steel microstructure on the hydrogen embrittlement phenomenon, Figure 24, Figure 25 and Figure 26 compare different diffusion (D_{app}, $D_{Lattice}$) and trapping parameters (E_a, N_T) among the studied steel grades.

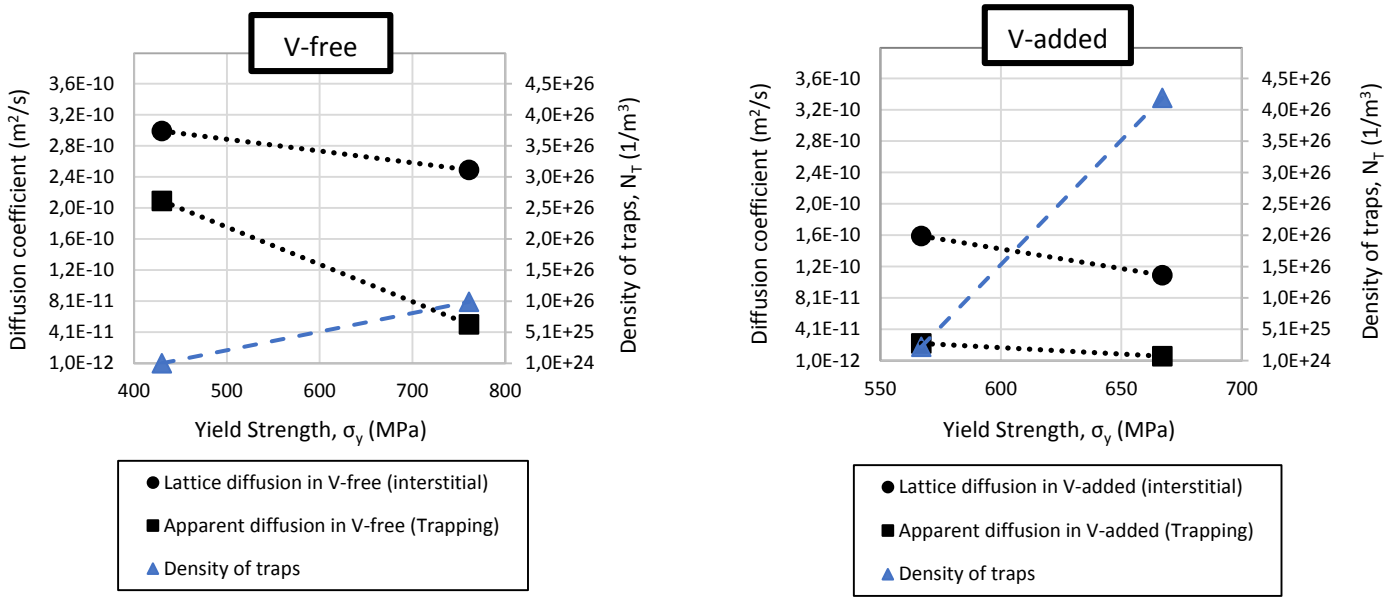

(a) (b)

Figure 24. Effect of tempering temperature on the hydrogen diffusion kinetics. (a) V-free grades. (b) V-added grades

Regarding the V-free grades, as yield strength increases (lower tempering temperature), the density of traps also increase and then, the apparent diffusion coefficient, D_{app}, decreases (see Figure 24a). A similar effect was observed in the V-added steel grades (see Figure 24b). It is also worth noting that the estimated apparent diffusion coefficient in the V-added grades was around one order of magnitude lower than the ones obtained in the V-free grades.

For example, in order to study the influence of vanadium addition on hydrogen diffusion, 2.25Cr1Mo_690 and 2.25Cr1MoV_720 can be compared, taking into account that the applied heat treatments had a similar Hollomon-Jaffe paramenter, P=20682 and P=20334 respectively. Nevertheless, due to the addition of vanadium and the precipitation of submicrometric vanadium carbides, the estimated trap density in the 2.25Cr1MoV_720 grade was around $2.3 \cdot 10^{25}$ sites/m^3, while it was much lower in the 2.25Cr1Mo_690 grade, $1.1 \cdot 10^{24}$ sites/m^3. Moreover, due to its higher density of traps, the V-added grade showed a hydrogen diffusion coefficient (D_{app}) around ten times lower than the 2.25Cr1Mo_690 grade. This behavior was also corroborated taking into account the activation energy of the stronger traps determined in the 2.25Cr1MoV_720 grade, 35 kJ/mol (desorption from V-carbides) compared to that obtained in the case of the 2.25Cr1Mo_690, 18 kJ/mol (Figure 25). In this same context and regarding the hydrogen permeation kinetics, it is also worth noting the strong delay of the hydrogen build-up permeation transient (Figure 26)

due to the V-addition (strong hydrogen traps). A similar effect is also observed when 2.25Cr1Mo_600 and 2.25Cr1MoV_650 are compared.

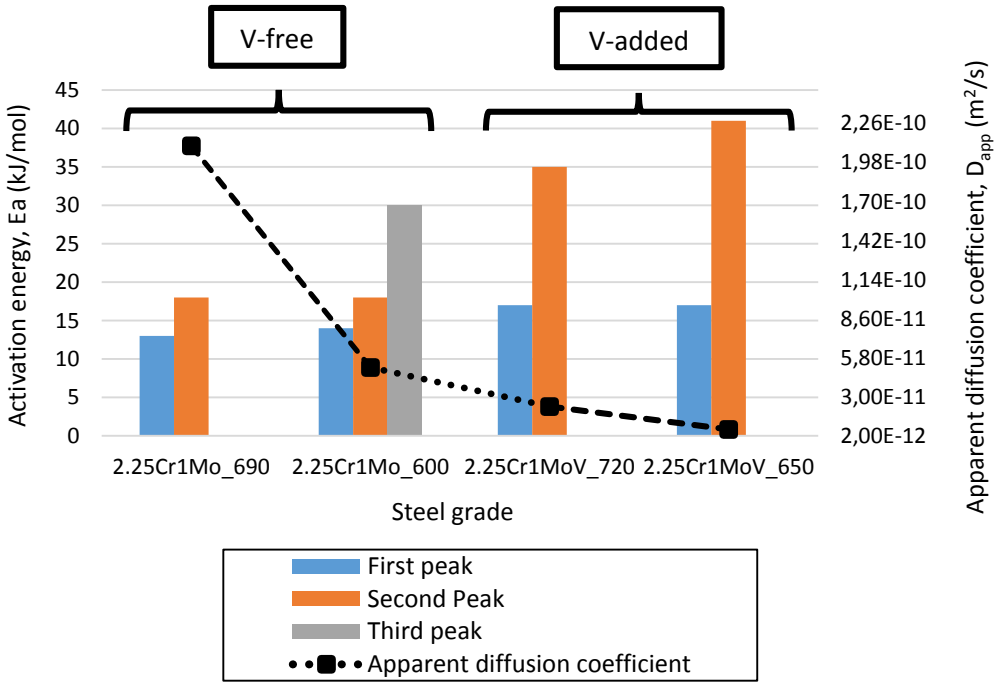

Figure 25. Effect of the vanadium addition on the apparent hydrogen diffusion coefficient and on the activation energies of hydrogen traps

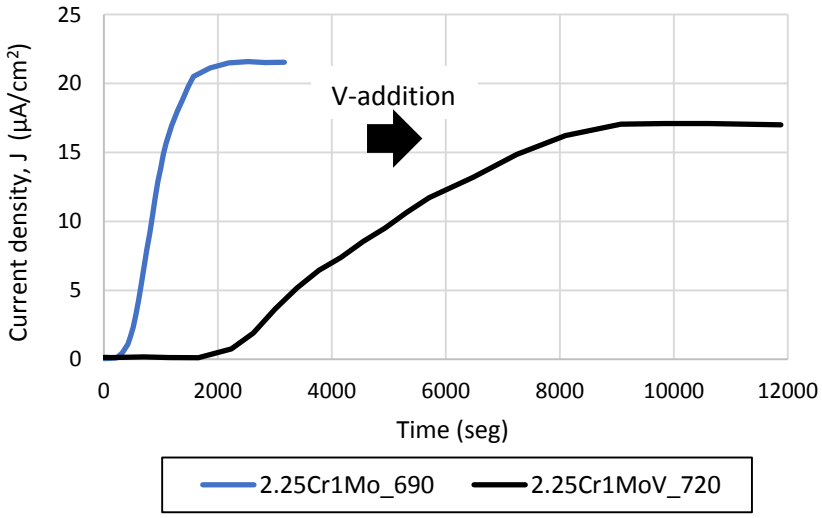

Figure 26. Effect of vanadium addition on hydrogen permeation results (hydrogen build-up transient)

According to the aforementioned results, V-added grades show a strong hydrogen-trapping capability, which contribute to retard hydrogen diffusion toward the notch tip region. This fact is responsible of the the mechanical behaviour improvement observed in these steel grades (V-added) in presence of internal hydrogen.

Figure 27 depicts the evolution of the embrittlement indexes (regarding notched strength and reduction in area) with the applied displacement rate for the different steel grades. Embrittlement indexes increase in both steels (V-free and V-added) as the yield strength of the grade increases (lower tempering

temperature). Accordingly, to explain the influence of the strength level on hydrogen embrittlement, Table 12 gathers the diffusible hydrogen (C_{H0}-C_{Hf}) already shown in Table 7 and the estimated local hydrogen concentration reached on the notch tip region (equation 1) from the hydrostatic stress calculated in Figure 16c in the different steel grades at the moment of failure.

Steel grade	C_{H0}-C_{Hf} (ppm) from Table 7	σ_H (ppm) from Figure 16c	$C_{H\text{-notch}}$ (ppm)
2.25Cr1Mo_690	0.40	620	0.66
2.25Cr1Mo_600	0.70	900	1.45
2.25Cr1MoV_720	0.30	726	0.54
2.25Cr1MoV_650	0.40	870	0.81

Table 12. Estimation of the local hydrogen concentration on the notch tip region

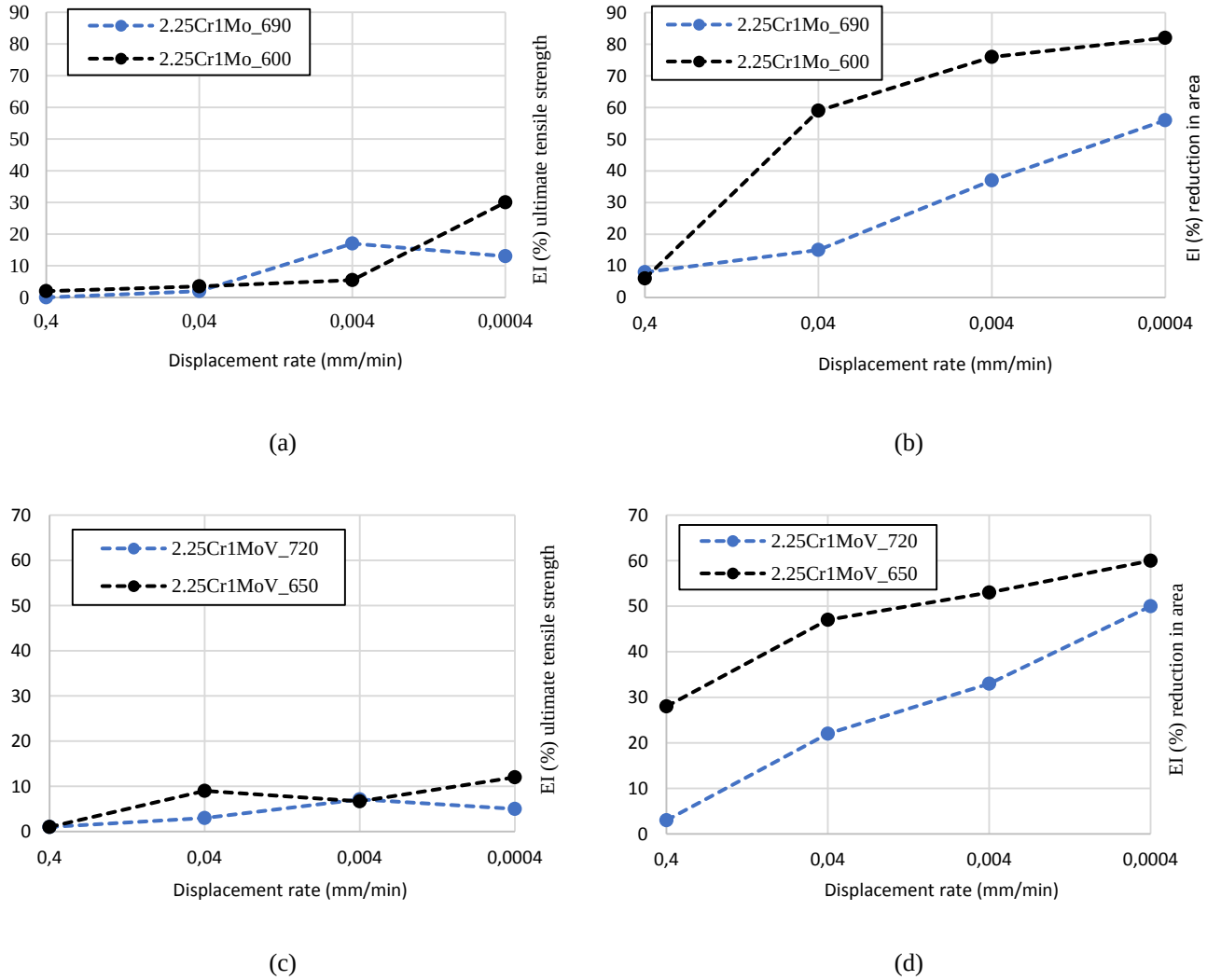

Figure 27. Embrittlement indexes on notched specimens depending on the displacement rate. (a)-(b) V-free steel grades and (c)-(d) V-added steel grades

As the MVC failure micromechanism was always the only failure mechanism observed in all the uncharged steel samples, the trend observed in Figure 27 is related with changes appreciated on the fracture micromechanisms (Table 11) due to the presence of internal hydrogen.

In the V-free steels, IG, PRHIC and cleavage micromechanisms were only observed in the grade with the highest yield strength (σ_y=761 MPa), while the steel tempered at the highest temperature (σ_y=430 MPa),

MVC was the predominant micromechanism, although some PRHIC areas were also observed in the periphery of the specimen tested at the lowest displacement rates. Considering that the internal hydrogen distribution is dominated by the hydrostatic stress and knowing that the highest hydrostatic stress in the notched tensile specimen is located just ahead of the notch tip, hydrogen will accumulate in this region. According with the results shown in Table 12, 1.45 ppm of hydrogen will be present on the process zone of the 2.25Cr1Mo_600 grade while hydrogen concentration on the process region at the moment of failure in the 2.25Cr1Mo_690 grade will be 0.66 ppm. In the former case, hydrogen accumulation will be enough to trigger cleavages and decohesion of the prior austenite grain boundaries (in general, hydrogen enhanced decohesion mechanisms, HEDE). On the other hand, as hydrogen accumulation in the process region of the grade with the lowest yield strength, 2.25Cr1Mo_690, was much lower, in this case the presence of internal hydrogen mainly provided plasticity localization on the notch region (HELP), giving rise to large and shallow dimples and only a small PRHIC area was detected in tests perfomed under the lowest displacement rates (Figure 18).

Regarding the V-added grades and independently of its stength level, intergranular fracture was never observed. In the grade tempered at the lowest temperature, 2.25Cr1MoV_650 (σ_y=667 MPa), hydrogen concentration into the process zone can attain 0.81 ppm and a peripheric region with PRHIC failure micromechanism and small cleavage areas were observed near to the notch tip region, although, large and shallow dimples were mostly observed in the rest of the fracture surface as a consequence of hydrogen enhanced localized plasticity (HELP). By the contrary, in the V-added CrMo steel tempered at 720ºC (σ_y=567 MPa), hydrogen accumulation into the process zone only attained 0.54 ppm, insufficient for the development of cleavage and PRHIC mechanisms, and only signals of hydrogen enhanced localized plasticity (HELP), with large and shallow dimples, were seen under all the applied displacement rates.

As a final summary, Figure 28 compares the embrittlement indexes evolution with the yield strength on V-free and V-added steel grades under a displacement rate of 0.0004 mm/min, where the highest embtrittlement indexes (EI) were noticed: the positive effect of vanadium addition is highlighted.

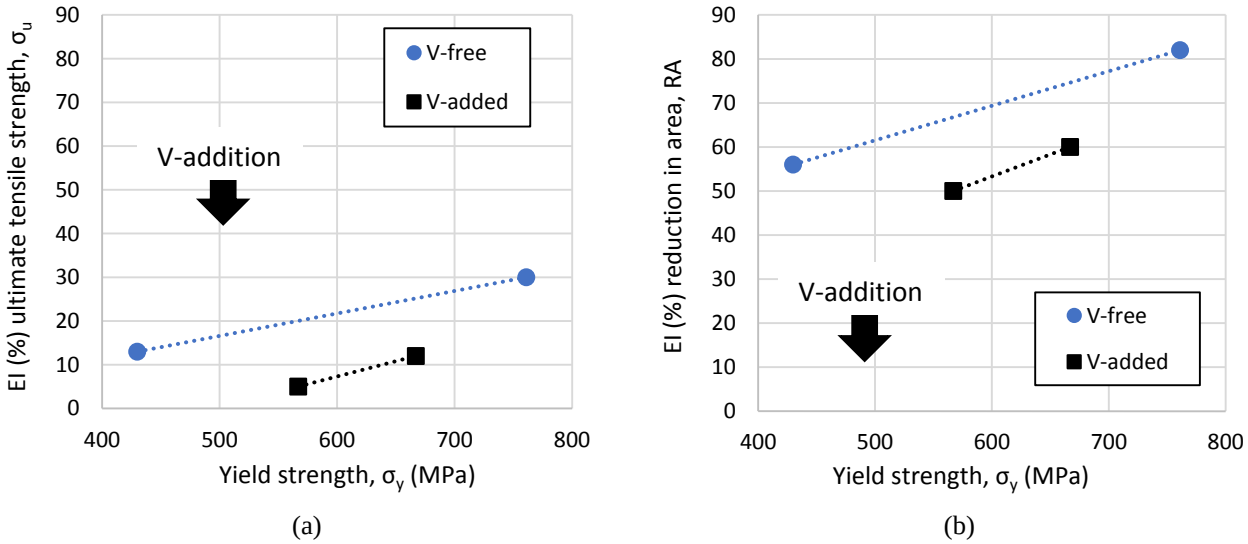

(a) (b)

Figure 28. Embrittlement indexes measured under the lowest displacement rate (0.0004 mm/min) with notched tensile specimens (Kt=4.25). (a) EI(%) in the ultimate tensile strength (σ_u) and (b) EI(%) in the reduction in area (RA)

V-added CrMo steel grades have a uniform dispersion of submicrometric vanadium carbides which act as strong traps for hydrogen, significantly reducing its mobility (see Figure 25). In these cases, despite having absorbed high hydrogen concentrations, around 4 ppm, only 10% of such hydrogen is able to diffuse along the steel microstructure to reach the process zone and this local concentration is barely able to trigger the most degrading embrittling mechanisms (cleavage, interface decohesion and intergranular fracture).

5 Conclusions

The results of the present work support the following conclusions regarding the hydrogen desorption kinetics, trapping and embrittlement under tensile loads of 2.25Cr1Mo(V) steel grades:

The initial hydrogen content increased in the V-added CrMo steel grades due to the fact that submicrometric vanadium carbide precipitates are very strong hydrogen traps. Regarding the V-free grades, the content of hydrogen strongly trapped in the microstructure decreased with increasing tempering temperature, mainly due to stress relaxation and the reduction in dislocation density and internal interfaces (martensite laths, blocks and packets).

Two hydrogen traps, with activation energies of 13-14 kJ/mol and 18 kJ/mol, were detected on the V-free grades tempered at high temperature and a third one with a higher activation energy of 30 kJ/mol was found in the grade tempered at lower temperature as the dislocation density of this grade was much higher (hydrogen trapped in dislocations). Hydrogen traps with higher activation energies around 35-41 kJ/mol were determined in the V-added steel grades, which were attributed to vanadium carbides precipitated along dislocations during the tempering treatment. Diffusible hydrogen and also the apparent hydrogen diffusion coefficient were much lower in the V-added grades.

The tensile properties measured on hydrogen pre-charged smooth specimens remained practically unaffected, even when tests were performed at the lowest displacement rates.

The embrittlement indexes (strength and reduction in area) obtained in hydrogen pre-charged notch tensile specimens always increase with the steel yield strength (increase dislocation density and residual stresses). The use of lower displacement rates always gave rise to higher embrittlement indexes, as the accumulation of hydrogen atoms in the process zone of the notched specimen increases due to the availability of longer diffusion times. These trends were consistent with changes appreciated in the fracture micromechanisms, from HELP (MVC, with large and shallow dimples) in the most resistant grades to HEDE (intergranular fracture, PRHIC and cleavage) for the grades most affected by hydrogen embrittlement.

V-added CrMo steel grades have a uniform dispersion of submicrometric vanadium carbides, which act as strong traps for hydrogen and, despite a larger absortion of hydrogen, diffusible hydrogen and hydrogen accumulation in the process zone of the notch tensile specimen decrease, giving rise to a significant better mechanical performance in the presence of internal hydrogen.

Acknowledgements

The authors would like to thank the Spanish Ministry of Economy and Competitiveness for the support received to carry out research Project MAT2014-58738-C3 (SAFEHIDROSTEEL).

References

[1] R.P.Gangloff , B.P.Sommerday. 'Gaseous hydrogen embrittlement of materials in energy technologies'. Volume 1: The problem, its characterisation and effects on particular alloy classes. Woodhead Publishing, 2012.

[2] L.Briottet, R.Batisse, G. de Dinechin, P.Langlois, L.Thiers. 'Recommendations on X80 steel for the design of hydrogen gas transmission pipelines'. International Journal of Hydrogen Energy, Volume 37, Issue11, 2012, 9423–9430.

[3] M.Wang, E.Akiyama, K.Tsuzaki. 'Effect of hydrogen on the fracture behavior of high strength steel during slow strain rate test'. Corrosion Science, Volume 49, Issue 11, 2007, 4081–4097.

[4] J.Yamabe, H.Matsunaga, Y.Furuya, S.Hamada, H.Itoga, M.Yoshikawa, E.Takeuchi, S.Matsuoka. 'Qualification of chromium-molybdenum steel based on the safety factor multiplier method in CHMC1-2014'. International Journal of Hydrogen Energy, Volume 40, Issue 1, 2015, 717-728.

[5] E.Akiyama, M.Wang, S.Li, Z.Zhang, Y.Kimura, N.Uno, K.Tsuzaki. 'Studies of evaluation of hydrogen embrittlement property of high-strength steels with consideration of the effect of atmospheric corrosion'. Metallurgical and Materials Transactions A: Physical Metallurgy and Materials Science, Volume 44, Issue 3, 2013, 1290-1300.

[6] D.K.Singh, R.K.S.Raman, S.K.Maiti, T.K.Bhandakkar, S.Pal. 'Investigation of role of alloy microstructure of AISI 4340 steel using circumferentially notched cylindrical specimens'. Material Science and Engineering A: Structural Materials, Volume 698, 2017, 191-197.

[7] L.B.Peral, A.Zafra, J.Belzunce, C.Rodríguez. 'Effects of hydrogen on the fracture toughness of CrMo and CrMoV steels quenched and tempered at different temperatures'. International Journal of Hydrogen Energy, Volume 44, Issue 7, 2019, 3953-3965.

[8] A.Zafra, L.B.Peral, J.Belzunce, C. Rodriguez. 'Effect of hydrogen on the tensile properties of 42CrMo4 steel quenched and tempered at different temperatures'. International Journal of Hydrogen Energy, Volume 43, 2018, 9068-9082.

[9] G.Álvarez, L.B.Peral, C.Rodríguez, T.E.García, F.J.Belzunce. 'Hydrogen embrittlement of structural steels: Effect of displacement on the fracture toughness of high-pressure hydrogen pre-charged samples'. International Journal of Hydrogen Energy, Volume 44, Issue 29, 2019, 15364-15643.

[10] R.A.Oriani, P.H.Josephic. 'Effects of Hydrogen on the plastic properties of medium-Carbon steels'. Metallurgical Transactions A , Volume 11, 1980, 1809-1820.

[11] H.Asahi, D.Hirakami, S.Yamasaki. 'Hydrogen trapping behavior in vanadium-added steels'. ISIJ International, Volume 43, Issue 4, 2003, 527-533.

[12] S. Yamasaki, T. Takahashi, 'Evaluation method of delayed fracture property of high strength steels'. Tetsu-to-Hagane, 83, 1997, 454-459.

[13] J.Lee, T.Lee, Y.J.Kwon, D.J.Mun, J.YYoo, C.S.Lee. 'Effects of vanadium carbides on hydrogen Embrittlement of Tempered Martensitic Steel'. Metals and Materials International, Volume 22, Issue 3, 2016, 364-372.

[14] Longfei Li, Bo Song, Jin Cheng, Zhanbing Yang, Zeyun Cai. 'Effect of Vanadium precipitates on hydrogen trapping efficiency and hydrogen induced cracking resistance in X80 pipeline steel'. International Journal of Hydrogen Energy, Volume 43, Issue 36, 2018, 17353-17363.

[15] I.Maroef, D.L.Olson, M.Eberhart, G.R.Edwards. 'Hydrogen trapping in ferritic steel weld metal', International Materials Reviews, Volume 47, Issue 4, 2012, 191-223.

[16] H.K.D.H. Badeshia. 'Prevention of hydrogen embrittlement in steels', ISIJ International, Volume 56, Issue 1, 2016, 24-36.

[17] J.Y.Lee and J.L. Lee. ‘A trapping theory of hydrogen in pure iron’. Philosophical Magazine A, Volume 57, Issue 3, 1987, 293-309.

[18] L.Jemblie, V.Olden, O.M.Akselsen. ‘A couple diffusion and cohesive zone modelling approach for numerically assessing hydrogen embrittlement of steel structures’, International Journal of Hydrogen Energy, Volume 42, Issue 16, 2017, 11980-11995.

[19] G.L.Spencer, D.J.Duquette. ‘The role of vanadium carbide traps in reducing the hydrogen embrittlement susceptibility of high strength alloy steels’. Technical report ARCBB-TR-98016, US Army Armament Research, N.Y. 1998.

[20] Ji Soo Kim, You Hwan Lee, Duk Lak Lee, Kyung-Tae Park, Chong Soo Lee. ‘Microstructural influences on hydrogen delayed fracture of high strength steels’. Materials Science and Engineering: A, Volume 505, Issues 1-2, 2009, 105-110.

[21] D.Li, R.P.Gangloff, J.R.Scully. ‘Hydrogen trapping states in ultrahigh-strength AERMET 100 steel’. Metallurgical and Materials Transactions A, Volume 35, 2004, 849-864.

[22] A.R.Troiano. ‘The role of hydrogen and other intersticials in the mechanical behaviour of metals’. Metallography, Microstructure and Analysis, Volume 5, Issue 6, 2016, 557-569.

[23] C.J McMahon. ‘Hydrogen-induced intergranular fracture of steels’. Engineering Fracture Mechanics, Volume 68, Issue 6, 2001, 733-788,

[24] S.K.Dwivedi, M.Vishwakanma. ‘Hydrogen embrittlement in different materials: A review’. International Journal of Hydrogen Energy, Volume 43, Issue 46, 2018, 21603-21616.

[25] H.K. Birnbaum, P. Sofronis. ‘Hydrogen-enhanced localized plasticity-a mechanism for hydrogen related fracture’. Materials Science and Engineering: A, Volume 176, Issues 1-2, 1994, 191-202.

[26] T.Depover, K.Verbeken. ‘The detrimental effect of hydrogen at dislocations on the hydrogen embrittlement susceptibility of Fe-C-X alloys: An experimental proof of the HELP mechanism’. International Journal of Hydrogen Energy, Volume 43, Issue 5, 2018, 3050-3061.

[27] A.Nagao, C.D.Smith, M.Dadfarnia, P.Sofronis, I.M.Robertson. ‘Interpretation of Hydrogen-induced Fracture Surface morphologies for Lath Martensitic Steel’. Procedia Materials Science, Volume 3, 2014, 1700-1705.

[28] I.M.Robertson, P.Sofronis, A.Nagao, M.L.Martin, S.Wang, D.W.Gross, K.E.Nygren. ‘Hydrogen embrittlement understood’. Metallurgical and Materials Transaction B: Process Metallurgy and Materials Processing Science, Volume 46, Issue 3, 2015, 1085-1103.

[29] S.Wang, M.L.Martin, P.Sofronis, S.Ohnuki, N.Hashimoto, I.M.Robertson. ‘Hydrogen-induced intergranular failure of iron’. Acta Materialia, Volume 69, 2014, 275-282.

[30] A.Oudriss, A.Fleurentin, G.Courlit, E.Conforto, C.Berziou, C.Rébéré, S.Cohendoz, J.M.Sobrino, J.Creus, X.Feaugas. ‘Consequence of the diffusive hydrogen contents on tensile properties of martensitic steel during the desorption at room temperature’. Materials Science Engineering A, Volume 598, 2014, 420-428.

[31] UNE-EN ISO 6506-1. Materiales metálicos. Ensayos de dureza Brinell. Parte 1: Método de ensayo, 2014.

[32] G.K.Williamson, W.H.Hall. ‘X-Ray line broadening from filed aluminium and wolfram’. Acta Metallurgica, Volume 1, Issue 1, 1953, 22-31.

[33] G.K Williamson, R.E Smallman. ‘Dislocation densities in some annealed and cold worked metals from measurements on the X-ray debye-scherrer spectrum’. Philosophical Magazine: A Journal of Theoretical Experimental and Applied Physics, Volume 1, 1956, 34-46.

[34] M.N.Yoozbashi, S.Yazdani. ‘XRD and TEM study of bainitic ferrite plate thickness in nanostructured, carbide free bainitic steels’. Materials Chemistry and Physics, Volume 160, 2015, 148-154.

[35] M.E.Fitzpatrick. ‘Determination of Residual Stresses by X-ray Diffraction’. Measurement Good Practice Guide No 52. Issue 2, 2005.

[36] ASTM G146. ‘Evaluation of disbonding of bimetallic stainless alloy/steel plate for use in high pressure, high temperature refinery hydrogen service’. In: Annual Book of ASTM Standards, vol. 03.02; 2013.

[37] M.A.V.Devanathan, Z.Stachursky. ‘The Adsorption and Diffusion of Electrolytic Hydrogen in Palladium’. Proceedings of the Royal Society of London. Series A, Mathematical and Physical Sciences, Volume 270, Issue 1340, 1962, 90-102.

[38] ASTM G148-97. ‘Standard practice for evaluation of hydrogen uptake, permeation and transport in metals by an electrochemical technique’, 2011.

[39] C.F. Dong, X.G. Li, Z.Y Liu, Y.R Zhang. ‘Hydrogen induced cracking and healing behaviour of X70 steel’. Journal of Alloys and Compounds, Volume 484, Issues 1-2, 2009, 966-972.

[40] T. Zakroczymski. ‘Adaptation of the electrochemical permeation technique for studying entry, transport and trapping of hydrogen in metals’. Electrochimica Acta, Volume 51, Issue 11, 2006, 2261-2266.

[41] S. Frappart, J. Creus, L. Delattre, X. Feaugas, F. Thebault, H. Marchebois. ‘Study of the hydrogen diffusion and segregation into Fe-C-Mo martensitic HSLA steel using electrochemical permeation test’. Journal of Physics and Chemistry of Solids, Volume 71, Issue 10, 2010, 1467-1479.

[42] N. Parvathavarthini, S. Saroja, R.K. Dayal. ‘Influence of microstructure on the hydrogen permeability of 9%Cr1%Mo ferritic steel’. Journal of Nuclear Materials, Volume 264, Issues 1-2, 1999, 35-47

[43] S.Pillot, L.Coudreuse. ‘Hydrogen-induced disbonding and embrittlement of steels used in petrochemical refinining’. Woodhead Publishing Limited, France, 2012.

[44] Krauss George. Steels: processing, structure and performance. 2005.

[45] B. De Cooman, J.G.Speer. ‘Fundamentals of steel product physical metallurgy’. Association for Iron and Steel Technology, 2008, Warrendale, PA, USA.

[46] L.B.Peral, A.Zafra, S.Blasón, C.Rodríguez, J.Belzunce. ‘Effect of hydrogen on the fatigue crack growth rate of quenched and tempered CrMo and CrMoV steels’. International Journal of Fatigue, volume 120, 2019, 201-214.

[47] A. Nagao, K.Hayashi, K.Ol, S.Mitao. ‘Effect of uniform distribution of fine cementite on hydrogen embrittlement of low carbon martensitic steel plates’. ISIJ International, Volume 52, 2012, 213-221.

[48] G.W.Hong, J.Y.Lee. ‘The measurement of the trap binding energy by the thermal analysis technique’. Scripta Metallurgica, Volume 17, Issue 7, 1983, 823-826.

[49] D.G.Enos, J.R.Scully. ‘A critical-strain criterion for hydrogen embrittlement of cold-drawn, ultrafine pearlitic steel’. Metallurgical and Materials Transactions A, Volume 33, 2002, 1151-1166.

[50] K.Takasawa, R.Ishigaki, Y.Wada, R.Kayano. ‘Absorption of hydrogen in high-strength low-alloy steel during tensile deformation in gaseous hydrogen’. ISIJ International, Volume 97, Issue 5, 2011, 288-294.

[51] T.Yokota, T.Shiraga, ‘Evaluation of hydrogen content trapped by vanadium precipitates in a steel’. ISIJ International, Volume 43, Issue 4, 2003, 534-538.

[52] K.Kiuchi, R.B.McLellan, ‘The solubility and diffusivity of hydrogen in well-annealed and deformed iron’. Acta Metallurgica, Volume 31, Issue 7, 1983, 961-984.

[53] H.J.Grabke, E.Riecke. ‘Absorption and diffusion of hydrogen in steels’. Materials Technology, Volume 34, 2000, 331-342.

[54] Y.Takeda and C.J.McMahon. ‘Strain controlled vs stress controlled hydrogen induced fracture in a quenched and tempered steel’. Metallurgical Transactions A, Volume 12, 1981, 1255–1266.